The Influence of Microphysics Parameterizations on Medium-Range Forecasts of Jet-Level Waviness During the 2016-2017 Cold Season

---

by

Jessica R. Taheri

A thesis submitted in partial fulfillment of

the requirements for the degree of

Master of Science

Atmospheric and Oceanic Sciences

at the

University of Wisconsin – Madison

2018

ABSTRACT

The release of latent heat in the production of clouds and precipitation characterizing mid-latitude weather systems can exert a substantial impact on the downstream Rossby wave pattern. Recent work has demonstrated that the nature of these impacts is strongly dependent upon the manner in which cloud and precipitation processes are represented in numerical forecast models. Models approximate the processing of water substance within such disturbances using cloud microphysical parameterizations of varying complexity.

Much prior work has considered the impact of latent heat release in organized cloud systems in terms of its contribution to forecast errors in the phase and/or amplitude of individual synoptic waves. Such consideration overlooks a related but perhaps more fundamental question – namely, what is the impact of such latent heat release on the aggregate waviness of the evolving, larger-scale flow? We conduct experiments aimed at gaining insight into this question.

First, we run a daily quartet of low resolution, 120-h WRF-ARW simulations in which we vary the model's cloud microphysics, cumulus and boundary layer parameterizations between the runs. Next, we employ sinuosity as a measure of the aggregate 200 hPa waviness over the Northern Hemisphere and consider the waviness differences in the light of the varying physical parameterizations in the model. A comparison of medium-range forecasts from the maximum and minimum waviness episodes from the 2016-17 Northern Hemisphere cold season is made. The analysis reveals that medium-range forecasts of waviness are most sensitive to the choice of cloud microphysics parameterization and that variation among the several cumulus parameterizations is dominantly controlled by the choice of microphysics package. In addition, it appears that a microphysical package of intermediate complexity renders the most accurate medium-range forecasts of jet-level waviness.

Thesis Declaration and Approval

I, Jessica R. Taheri, declare that this thesis titled ‘The Influence of Microphysics Parameterizations on Medium-Range Forecasts of Jet-Level Waviness During the 2016-2017 Cool Season” and the work presented in it are my own.

Jessica R. Taheri___ ______________________________ ____________
Author Signature Date

I hereby approve and recommend for acceptance this work in partial fulfillment of the requirements for the degree of Master of Science:

Jonathan E. Martin__ ______________________________ ____________
Committee Chair Signature Date

Michael Morgan____ ______________________________ ____________
Faculty Member Signature Date

Brett Hoover_______ ______________________________ ____________
Committee Member Signature Date

ACKNOWLEDGEMENTS

First and foremost, I'd like to thank Dr. Jonathan E. Martin for inspiring me to want to return to school and earn my Master's degree in Atmospheric and Oceanic Sciences. During my undergraduate studies in my Dynamics I and II and Synoptic Meteorology classes, we learned from your book and I was hooked from page one. When I decided to return to graduate school, I knew based on how much I enjoyed learning from your book that I was the most passionate about atmospheric dynamics or synoptic meteorology and I set my sights on working with you at the University of Wisconsin – Madison. I am so honored to have your name on my thesis as my primary adviser, and sometimes I still cannot believe I spent the last three years working for and with you. I have enjoyed every second. I cannot thank you enough for giving me this opportunity to study under you and build on your research ideas. Thanks to your support in my studies and encouragement to follow my own career path, you have once again proven to me that I couldn't have asked for a better adviser through this process. Thank you, thank you, thank you!

Thanks, also to Dr. Samuel Stechmann and Dr. Leslie Smith who also played crucial roles in this project. Your support from the math department aided in funding this project and your ideas helped fuel the work I've completed. In addition, I'd like to thank Alfredo Wetzel and Thomas Edwards for your work as it relates to atmospheric sciences.

There are many other colleagues/friends who have played a major role in shaping this thesis as you read it now: Dr. Michael C. Morgan, Dr. Brett Hoover, Dr. Melissa Breeden, Maria Madsen, Alex Goldstein, Dr. Zak Handlos, Dr. Kyle Griffin, Simran Raju, Connor Dacey, Zoe Brooke-Zibton and Craig Oswald. I would specifically like to thank

Dr. Michael Morgan and Dr. Brett Hoover for being on my MS committee. Your comments, feedback, and edits were invaluable. I'd also like to thank Dr. Morgan for your continued guidance with the WRF and willingness to answer any questions—whether they were related to your class or not—and for your numerous suggestions and ideas as they related to my research.

There are so many people outside of this department and building who helped keep me sane through these last few years. Without their support and encouragement, I wouldn't be finishing my thesis and starting my career. First, I'd like to thank my mom, Belinda Taheri, who answered every call at every hour to help me through every project and class and who was always excited for me when my research and coding went right (even though she didn't understand a word I said) and helped me to continue to believe in myself when things got hard. Second, I'd like to thank my dad, Arman Taheri, who was so proud of me when I got accepted into Wisconsin (I think our football/basketball team records helped) and was always was willing to lend an ear and offer advice when I needed it. Also, I'd like to thank my siblings: AJ, Hannah and Tristan. You guys are truly the best and coming home to see you (and the dogs) always gave me the perfect recharge I needed to keep going with my work.

Another person I'd like to personally thank profoundly is Jack Gayer. When you agreed to move to Wisconsin with me we had no idea that the last three years would be the hardest of your life, yet—without fail—you were *always* there for me. I couldn't have done this without your continuous support, confidence in me, and presence. From the bottom of my heart, thank you for your unconditional love through this venture. I appreciate it more than you know and I don't think you'll ever grasp just how much your encouragement and support contributed to my successful completion of this thesis.

To my Aunt Danette and Uncle Robert, thank you for all your support and career advice and for becoming my Madison landlords so I would have wouldn't have to live in crooked houses with broken windows. And to the many strong, female role models in my life, you inspire me to set my sights high and never back down from a challenge.

Finally, I'd like to thank the many lifelong friends I met along the way here in Madison: Karlyn Schumacher, Erwin Herrera, Katie and Tanya Ballinger, Joseph Nettesheim, and Andrew Dzambo. You are all proof that whoever says that Craigslist and brewery tours aren't the kinds of places to find lifelong friends is just plain wrong.

Sometimes I still need to pinch myself as a reminder of how lucky I am that I've had the privilege of continuing my education at the University of Wisconsin – Madison. From the second I decided I wanted to return to school, I knew I had my sights set on attending UW–Madison and working with Jon. Every day when I walk into "that tall building with all the satellites on top" I still cannot believe it's something I get to do, and I take so much pride in including such a prestigious, reputable program on my resume under the guidance of, arguably, one of the best meteorologists and forecasters in our field. I am forever a UW alumna, terrace-lover, cheese head, badger and, of course, a proud Sconnie. On, Wisconsin!

This work was supported by NSF Grant AGS-1443325.

TABLE OF CONTENTS

i. List of Figures

ii. List of Equations

iii. List of Abbreviations

ACM2	**A**symmetric **C**onvection **M**odel **2**
AMS	**A**merican **M**eteorological **S**ociety
ARW	**A**dvanced **R**esearch **W**RF
AR	**A**tmospheric **r**iver
BMJ	**B**etts-**M**iller-**J**anjic
CU	**Cu**mulus
CW3E	**C**enter for **W**estern **W**eather and **W**ater **E**xtremes
hPa	**H**ecto**pa**scals
HRRR	**H**igh **R**esolution **R**apid **R**efresh
HWRF	**H**urricane **W**eather **R**esearch and **F**orecast
KF	**K**ain-**F**ritsch
MCS	**M**esoscale **C**onvective **S**ystem
MP	**M**icro**p**hysics
MYJ	**M**ellor-**Y**amada-**J**anjic
NAWDEX	**N**orth **A**tlantic **W**aveguide and **D**ownstream Impact **Ex**periment
NCAR	**N**ational **C**enter for **A**tmospheric **R**esearch
NCDC	**N**ational **C**limatic **D**ata **C**enter
NCEP	**N**ational **C**enters for **E**nvironmental **P**rediction
NOAA	**N**ational **O**ceanic and **A**tmospheric **A**dministration
NOLH	**No** **l**atent **h**eat
NWP	**N**umerical **W**eather **P**rediction

PBL	**P**lanetary **B**oundary **L**ayer
PV	**P**otential **V**orticity
SAS	Old **S**implified **A**rakawa-**S**chubert
WCB	**W**arm **c**onveyor **b**elt
WRF	**W**eather **R**esearch and **F**orecast
YSU	**Y**on**s**ei **U**niversity

1. INTRODUCTION

Within numerical weather prediction (NWP) models, a variety of physical processes must be *parameterized*, or approximated by closure assumptions and derived from the model state rather than calculated explicitly, because they are highly non-linear, unresolvable at model scale, or both. Parameterization impacts both the fidelity of the forecast and the depiction of the dynamics of the evolving atmospheric flow as the effect of sub-grid-scale processes grows upscale to influence the flow at grid-scale. Due to the current state of computer processing, processes such as latent heat release, turbulence, entrainment, and boundary layer mixing, must be parameterized in order to approximately represent processes that occur on a spatial scale of 2 km or less. In this study, we are interested in the manner in which cloud processes on the microscale, such as growth, evaporation, and condensation of hydrometeors (and their depiction) affect the large-scale flow.

Although microphysical processes occur on scales that are orders of magnitude smaller than the mesoscale (a few to several hundred kilometers) or synoptic scale (hundreds of kilometers), these processes and their associated energy transformations are critical to understanding how weather systems develop and evolve. Since NWP modelers are typically designed for simulation from mesoscale to planetary scale, they often employ cloud microphysics schemes of varying complexity in an attempt to portray the phase changes between water and ice as accurately as possible. These phase changes can directly impact how weather systems develop, what intensity they attain, and their surface weather impacts, as well as downstream development. Thus, alterations in one parameterization scheme can have an influence on other model parameterizations and processes. For instance, a change in the planetary boundary layer scheme may induce changes in the manner by which radiation is treated which, in turn, can affect the production of cumulus cloud cover in the model through parameterized cumulus convection. Such a cascade of impacts can have a cumulative effect exerting substantial influence on the forecast. We will investigate the link between parameterized diabatic processes within cloud processes, specifically latent heat release, to the downstream synoptic-scale forecast waviness.

It is well known that diabatic processes, such as latent heat release, can impact Rossby wave structure, either by strengthening elements of the associated wave train or by altering the downstream flow waviness (Stoelinga, 1995; Pomroy and Thorpe, 2000; Massacand et al., 2001; Joos and Wernli, 2012; Chagnon et al., 2013; Madonna et al., 2014; Gram and Archambault, 2016; Joos and Forbes, 2016). Stoelinga (1995) showed that close to 70% of the strength of a mature surface cyclone could be attributed to latent heating and its subsequent effects of creating positive and negative potential vorticity (PV) anomalies at the surface and aloft, respectively. Chagnon et al. (2013) demonstrated that diabatic amplification of an upper-level PV wave can result in enhanced baroclinic wave growth of up to 10-20%. The impact of latent heating on the PV structure is well understood, but the downstream effects, in time, of such latent heating parameterizations on the evolving flow is less clear.

Recent studies have shown there is a link between choice in microphysics parameterization and effects on a variety of downstream forecast parameters. Tropical cyclone intensity and size have been shown to be sensitive to the selection of the microphysics scheme within a model (Chan and Chan, 2016). Dirren et al. (2003) showed that poor representation of the diabatic effects associated with a cyclone can lead to forecast error for that cyclone. In addition, such deficiencies impact the model depiction of tropospheric PV, leading to errors in the development of the Rossby wave amplitude, including a lack of streamer formation associated with wave breaking. These papers, as well as others, have investigated the impact that various parameterizations have on specific events, such as tropical and extratropical cyclones, extratropical transition, or the impact on phase/amplitude errors of individual synoptic waves, but not the impact on the overall hemispheric waviness.

This thesis centers on a comparison of a daily quartet of 120-hour WRF forecasts, each employing a different microphysics parameterization, run each day from 1 November 2016 to 31 March 2017. We specifically examine the 200 hPa aggregate waviness throughout each 5-day forecast employing a simple measure known as *sinuosity*, described in detail in Section 3.3. In this way, we determine which microphysics parameterization renders the most accurate medium-range forecasts of Northern Hemispheric waviness on average. Further experiments are run in a similar manner to examine the influence other parameterizations have on the waviness forecast. Finally, experiments in which both the microphysics and cumulus parameterizations are interchanged permit a comparison of the relative influences of these important parameterizations on forecasts of hemispheric waviness.

The rest of this thesis is organized as follows. In Chapter 2 a background and motivation are provided. Chapter 3 includes details regarding the WRF setup employed in the study, as well as introduction of the sinuosity metric. In Chapter 4, the results of varying microphysics and cumulus parameterizations on forecasts of 200 hPa aggregate sinuosity are presented. Finally, Chapter 5 provides a summary and conclusions, in addition to potential future work.

2. BACKGROUND

2.1 Potential Vorticity Modification of the Rossby Wave Structure

The mid-latitude atmosphere is full of large- and small-scale wave phenomena, some of which have a direct bearing on the development of the cyclones and anticyclones that parade around the hemisphere. The largest of these waves, colloquially known as Rossby waves, are an important component of many such developments. Among the several means of identifying and tracking these Rossby waves, the potential vorticity perspective is particularly amenable to gaining an understanding of how they are influenced by diabatic heating.

The PV in isentropic coordinates is given by:

$$\mathbf{PV} = -(\boldsymbol{\zeta_\theta} + \boldsymbol{f})\left(\frac{\boldsymbol{\partial\theta}}{\boldsymbol{\partial p}}\right) \tag{1}$$

where ζ_θ is the relative vorticity on a θ surface, *f* is the Coriolis parameter, and θ is the potential temperature. Neglecting friction, the Lagrangian time rate of change of the PV (Eq. 1) is:

$$\frac{\mathrm{D}}{\mathrm{Dt}}(\mathrm{PV}) = -\mathrm{g}\left(\vec{\eta}_a \cdot \nabla\dot{\theta}\right) \tag{2}$$

where g is the acceleration due to gravity, $\vec{\eta}_a$ is the 3-D absolute vorticity vector and $\dot{\theta}$ is the diabatic heating rate. For most flows of interest, the vertical gradient of diabatic heating rate dominates compared to the horizontal gradient, which reduces Eq. 2 to:

$$\frac{\mathbf{D}}{\mathbf{Dt}}(\mathbf{PV}) = -\mathbf{g}(\boldsymbol{\zeta_\theta} + \mathbf{f})\frac{\boldsymbol{\partial\dot{\theta}}}{\mathbf{\partial p}} \tag{3}$$

where $-\frac{\partial\dot{\theta}}{\partial p}$ is the vertical derivative of diabatic heating.

Using Eq. 3, it follows that positive (cyclonic) PV is generated below the level of maximum heating, and destroyed above, as illustrated in Fig. 1. The newly created PV anomalies can cause the enhancement of the local horizontal PV gradient, resulting in the strengthening (weakening) of a local ridge (trough) feature, an area of locally negative (positive) PV. Such destruction of PV above the level of maximum heating was central to the analysis of Stoelinga (1995) who showed that negative PV anomalies developed above the level of maximum heating, modifying the upper-level PV pattern downstream.

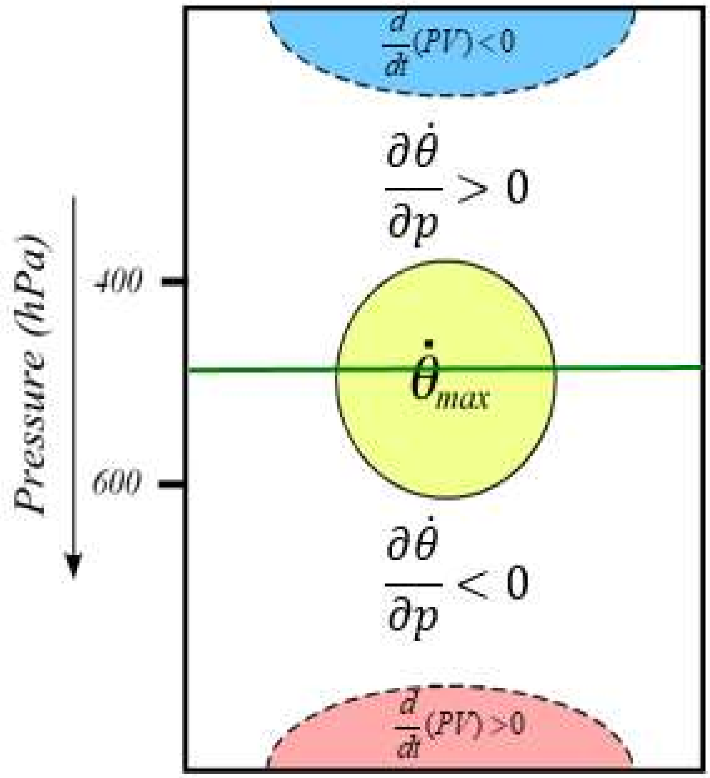

Figure 1: Showing regions where positive and negative PV are generated over time due to the influence of latent heat release (indicated by the level of maximum heating in the middle of the diagram) initialization in the Northern hemisphere.

A second way that latent heat release can impact the Rossby wave pattern is by diabatically generated PV altering the winds and in turn affecting the development of waves on the jet stream by affecting the PV gradient (Chagnon et al., 2013). Figure 2a shows an initial tropopause PV gradient remote from a convective element, represented by $\dot{Q}$ to signify its association with latent heat release. As the convection encroaches on the tropopause PV gradient, upper-level PV is eroded on the south side of the original gradient. As a result of this PV destruction, the horizontal gradient of PV in the vicinity of the convective element has increased. In Fig. 2b, the effects on the PV gradient in the upper troposphere and waveguide are shown: an induced horizontal circulation and a resulting alteration along the PV waveguide downstream.

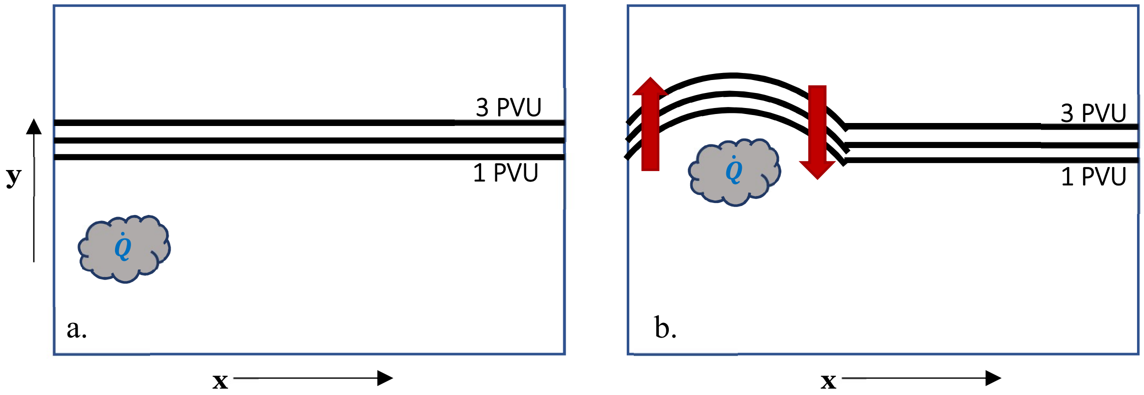

Figure 2: Solid black lines indicate the 1, 2, and 3 PVU (1.0×10^{-6} m^2 s^{-1} K kg^{-1}) isertels on the 330 K surface (~200 hPa). $\dot{\boldsymbol{Q}}$ represents the location of a cloud element. Red arrows represent the induced horizontal circulation on the flow due to the enhancement of the PV gradient.

There is another way in which parcels can impact the tropopause-level PV gradient. Though parcels below the level of maximum heating have positive PV tendency, once they are above the level of maximum heating through ascent, they acquire a negative PV tendency. Thus, even though the total integrated PV change along the parcel path may be small, the convergence of parcels with negative (anticyclonic) PV tendencies contributes to the upper-level accumulation of negative PV and can aid in the strengthening of the PV gradient along the tropopause if accumulation is equatorward of the jet. Parcel ascent on the large-scale is often associated with diabatic cloud formation and precipitation processes, thus leading to a potential for strong influence on the upper-level PV pattern, and amplification of ridges (Joos and Forbes, 2016). This process is most common in warm conveyor belts (WCBs), where a large number of parcels are undergoing ascent, and can contribute significantly to the negative PV anomaly located near the tropopause level. In areas where intense latent heat release is occurring, such as in a developing cyclone, atmospheric rivers (ARs), or WCBs, the impact on the PV gradient can be significant, and thus the structure of the jet and downstream features can be altered, leading to downstream forecast impacts, potentially on a global scale.

2.2 Downstream Impacts

As previously mentioned, the negative PV anomaly created by diabatic processes can lead to the enhancement of a local ridge and/or strengthening of the jet stream. Strengthening a local ridge through strengthening the PV gradient often leads to the downstream development of a trough which can lead to non-linear deformation of material contours, such as Rossby wave breaking. Figure 3 (adapted from Fig. 4 in Grams and Archambault, 2016) shows how downstream strengthening of features can occur through upstream latent heat release. In Fig. 3a and Fig. 3b, the flow is considered low-amplitude, as the latent heat release has just begun. In Fig. 3c and Fig. 3d, the amplitude of the trough (T2) and ridge (R1, R2) features downstream of the latent heat release starts to increase. Finally, in Fig. 3e, we can potentially identify a PV streamer (T2), as well as a blocking ridge (R2), both high amplitude, non-linear, and irreversible events which have developed as a result of the

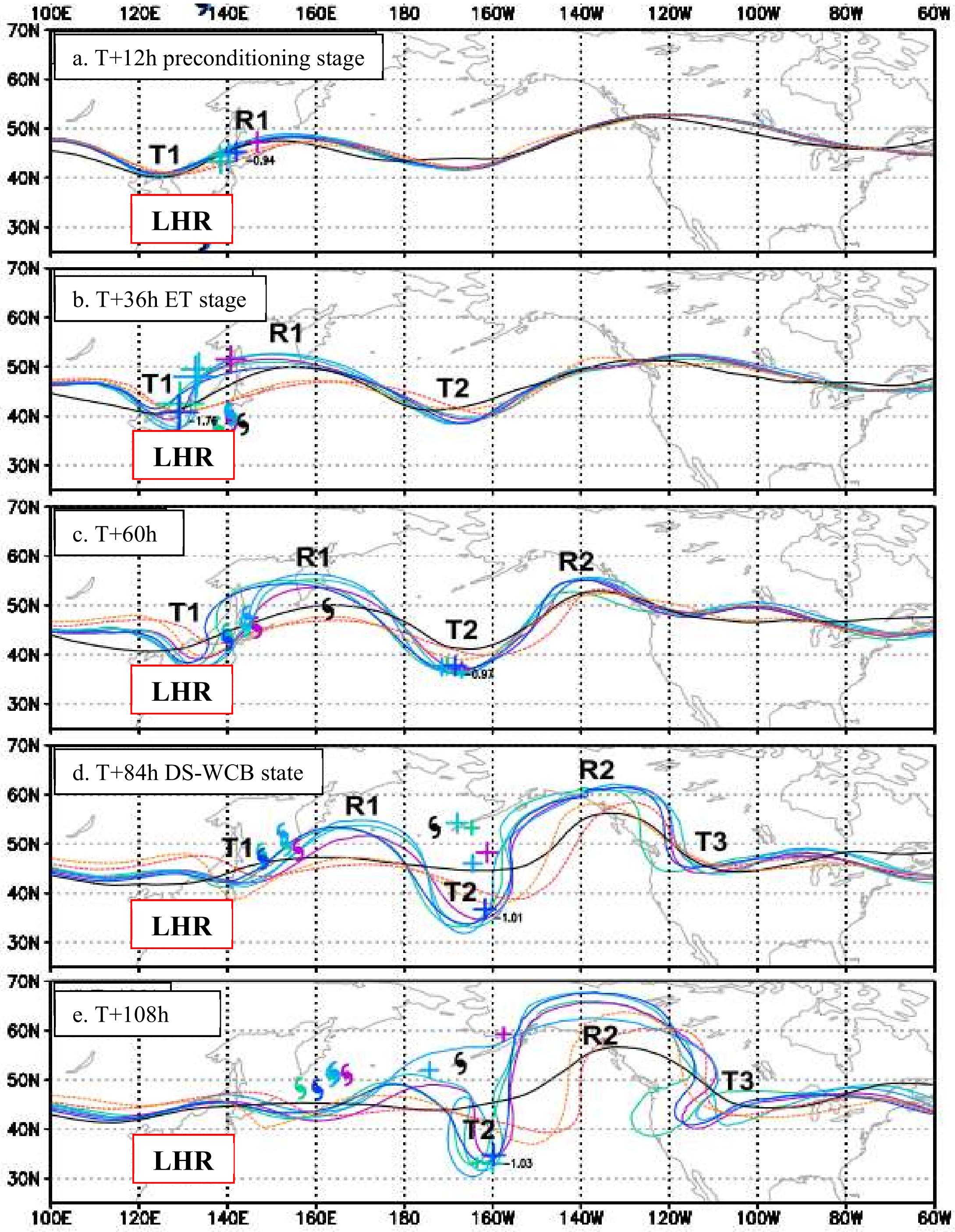

Figure 3: From Grams and Archambault, 2016 (their Fig. 4) showing the downstream impact on the 200 hPa flow due to the latent heat release added from a recurving tropical cyclone. The lines represent simulations of the same model run with varying latent heat or convective schemes. The location of the latent heat release is identified with "LHR". T1, R1, etc. represent "trough 1" and "ridge 1", respectively. Times indicate time from model initialization.

negative PV created due to the area of high latent heat release. This high amplitude flow can often manifest itself in the form of blocking, PV streamer development, as shown in Fig. 3, or formation of a cut-off low, as well as increased poleward moisture advection through ARs or WCBs (not shown in Fig. 3). Each of these phenomena has distinct, and sometimes extreme, impacts on the sensible weather experienced at the surface with the potential to bring significant impacts on life and property, and are thus important to accurately forecast. These events will be explained below.

2.2.1 Rossby Wave Breaking

There are two types of (Rossby) wave breaking events: deemed LC1 (anticyclonic) and LC2 (cyclonic) by Thorncroft et al. (1993), as shown in Fig. 4. During LC1 wave breaking, anticyclonic shear on the equatorward side of the jet causes a northeast-southwest oriented filament (Fig. 4a), often identified as a PV streamer, which can then break off into cut-off vortices (also known as cut-off lows). In LC2 wave breaking, the disturbance remains on the poleward side of the jet, and wraps up cyclonically, remaining relatively broad with no cutoffs forming (Fig. 4b) (Martius et al., 2007). Wave breaking can lead to a variety of impacts on the overall hemispheric Rossby wave structure, both locally as well as far downstream, such as the developing of a blocking ridge, PV streamers, and cut-off lows.

Atmospheric blocking refers to a large-amplitude, quasi-stationary anticyclone in the extratropics. These events occur on the synoptic-scale and can cover the entire depth of the troposphere, with potential to impact the flow at almost every vertical level. In the summer months, blocks can result in drought and anomalously warm temperatures throughout the troposphere. In the winter months, blocking can aid in the advection of polar air masses equatorward, leading to cold-air outbreaks. (Pfahl et al., 2015).

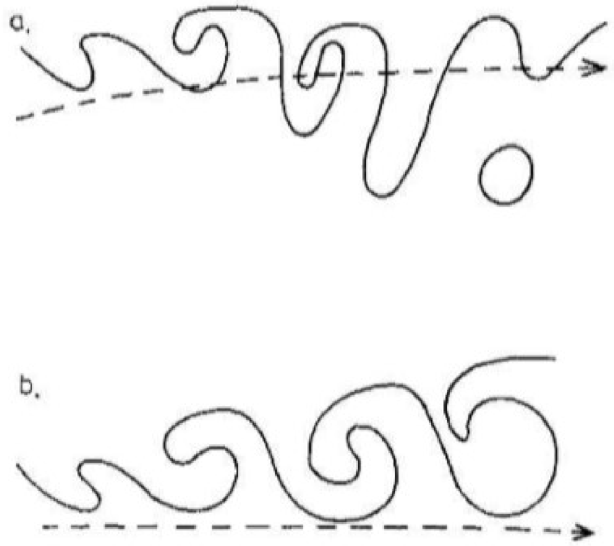

Figure 4: From Throncroft et al., 1993 (their Figure 12). Showing the PV-theta contour (solid) of (a) an LC-1 life cycle and (b) an LC2 life cycle and the approximate location of the mean jet (dashed).

Due to the large amplitude of these anticyclones, a trough similar in amplitude often develops upstream and/or downstream in response. These high-amplitude troughs, or PV streamers, are represented by thin, deformed areas of strong PV gradients on isentropic surfaces. LC1-type streamers can be viewed as positive upper-level PV anomalies, and are closely linked to surface weather patterns, such as active frontal zones and considerable precipitation production, as well as cyclogenesis and poleward moisture flux. Eventually these PV streamers undergo an irreversible process known as wave breaking, during which enhanced exchange between the stratosphere and troposphere can occur (Martius et al., 2007).

If a PV streamer becomes of high enough amplitude, a cut-off cyclone can develop. Cut-off cyclones are closed circulations with cold cores that are cut-off from the mean westerly flow. Their formation is an example of a process that can occur when the synoptic-scale Rossby wave flow reaches a point of significant instability within the troposphere. A cut-off forms when a high amplitude wave continues to deepen until it eventually detaches completely from the main zonal stream, as seen in the final time in Fig. 4a. Generally, the troposphere below the cut-off low is weakly stratified which leads to scattered convection, uneven precipitation distribution with moderate to heavy rainfall over large areas, and enhanced stratosphere-troposphere exchange aloft. Cut-off lows are often difficult to forecast, but can bring substantial surface weather impacts, particularly across southern Europe and northern Africa, where intense precipitation rates have led to catastrophic flooding events (Nieto et al., 2005).

2.2.2 Poleward Water Vapor Transport

Increased poleward water vapor transport is another common by-product of the formation of elongated troughs, such as PV streamers. The strongest magnitude of this water vapor transport is located close to the surface, often manifesting itself in the form of an AR or WCB; both of which have led to significant downstream events such as devastating flooding across the western United States and western Europe (Knippertz and Martin, 2006; Massacand et al., 1998).

Atmospheric rivers are defined as long (approximately 2000 km), and narrow (approximately 850 km) transient corridors of strong horizontal water vapor transport typically associated with a low-level jet ahead of the cold front of an extratropical cyclone

(Corderia et al., 2017). These features bring moist tropical air poleward, typically carrying integrated vapor transport values between 200-850 $\mathrm{kg\,m^{-1}\,s^{-1}}$. When ARs intercept enhanced topography, heavy rainfall, flooding, deep snow pack and mudslides can result. Landfalling ARs have been estimated to be responsible for up to 50% of annual precipitation along the west coast of the United States (Dettinger et al., 2014).

Warm conveyor belts are organized airstreams located ahead of the surface cold front in extratropical cyclones. These features transport warm, moist air from the lower-latitude boundary layer poleward before ascending rapidly over the cyclones warm front and contributing to the development of frontal clouds and precipitation (Knippertz and Martin, 2006). The action of a WCB, often manifest in the growth of the cloud head of an extratropical cyclone, can contribute to rapid storm development, possibly even explosive cyclogenesis (Eckhardt et al., 2004). Joos and Forbes (2016) found that small changes to the vertical location of WCB outflow could be attributed to different microphysics parameterizations of rainfall autoconversion and evaporation in a model. Since the dynamical impact of latent heat release is dependent on the level at which heating occurs this results hints at the importance microphysics parameterizations can have on model forecasts of precipitation as well as downstream flow evolution.

2.3 Parameterization of Water Process in Models

As discussed previously, the latent heat release within convective or widespread precipitation events can impact the planetary-scale waviness, and thus render a large impact on the broad synoptic environment. Consequently, correctly representing latent heat release and other aspects of phase changes delivers an important, but necessarily parameterized, impact on NWP forecasts ranging in scale from individual clouds to hemispheric waviness. Through its microphysics parameterizations, the way in which a model processes water vapor has an impact on the downstream forecast waviness and its embedded weather systems. Therefore, any model errors within high latent heat release events can lead to the translation of these errors downstream in the forecast. In a recent study, Rodwell et al. (2013) found that when mesoscale convective systems (MCSs) – which release a large amount of latent heat release over a relative small area – are present over the United States, higher forecast "bust" potential over Europe was observed in the six days following the MCS, particularly in forecasting a blocking ridge over Europe. In one case study conducted by the authors, the model physics played an active role in slowing down the evolution and development of a synoptic-scale trough, thus leading to a busted forecast over Europe. The authors speculated this bust was a result of the model errors in forecasting the precipitation location and intensity, thus mobilizing downstream errors that lead to the bust.

The manner by which a model parameterizes diabatic processes is crucial to the development and evolution of PV anomalies within the model forecast. If such features are not accurately simulated, forecast errors can result downstream (Chagnon et al., 2013). In a model, the strength and distribution of PV anomalies is partly determined by the microphysics processes used in the model, of which one can view latent heat release as a by-product (Joos and Forbes, 2016). This means that some portion of forecast downstream waviness in a model is dependent on the particular microphysics scheme used in a given simulation. Grams and Archambault (2016) showed increased downstream forecast errors were reported in NWP models in relation to extratropical transition. In their study, they concluded that the parameterization of diabatic processes, which is partly determined by the model's microphysics scheme, was likely the reason for these downstream errors. Gray et al. (2014) noted that errors in the representation of diabatic processes in global and regional weather forecast models can cause additional errors, such as forecast uncertainty and misrepresentation of systems downstream.

The inability to correctly parameterize diabatic heating intensity and location causes downstream errors which not only impact large-scale events, such as extratropical cyclones, but also smaller-scale events evolving from and embedded within the flow, including thunderstorms and locally heavy rain or snowfall, which can be a result of the trough structure and its embedded PV anomaly being situated in the wrong place or being of a different amplitude (Chagnon et al., 2013). Martinez-Alvarado et al. (2015) suggest that benefits of improving the parameterizations of diabatic processes also include extending NWP lead times, improved lateral boundary conditions for nested models and improved statistical properties of climate model runs. Thus, understanding the impacts of microphysics schemes on any aspect of the forecast will contribute to the understanding of how these parameters impact and interact with other model forecast components.

2.4 Current Research

Research into the downstream impacts of latent heat release and microphysics on Rossby waves, both through observations and model parameterizations, is expanding. The North Atlantic Waveguide and Downstream Impact Experiment (NAWDEX) conducted flight campaigns, which ended in October 2016, investigating how diabatic processes over North America and the North Atlantic can influence the jet stream and development of

Rossby waves causing high impact weather over Europe. Joos and Wernli (2012) investigated a selected WCB and the role of different microphysical processes in altering the diabatic heating rates and subsequent PV modification. Grams and Archambault (2016) found that negative PV advection by the diabatically driven flow in extratropical transition initiates ridge building and amplifies the overall Rossby wave pattern. Joos and Forbes (2016) found significant differences in the upper-level PV pattern resulted from changing the microphysics parameterizations within a model simulation of a WCB. All of these studies, as well as many others, involve either looking at the downstream impacts arising from a specific source of latent heat release, or the effects of upstream latent heat release on a specific downstream event. In this study we aim to evaluate the impact of model microphysics parameterizations on the aggregate hemispheric waviness, defined by sinuosity (see Section 3.3).

3. DATA AND METHODS

3.1 Weather Research and Forecasting (WRF) Model

The Weather Research and Forecasting (WRF) model is a product of a collaborative effort involving a number of national centers and universities to create an atmospheric model designed to advance the understanding and prediction of weather. It was created with the intent to be flexible, state-of-the-art, and portable, to be run on laptops or supercomputers, serving the broad meteorological community through research and operational applications. The WRF is maintained and supported as a community model, with over 39,000 WRF registered users[1].

The Advanced Research WRF (ARW) is a subset of the larger WRF system. The ARW dynamic solver works in conjunction with a range of numerical and dynamical options, data assimilation and initialization routines to run the model. The ARW dynamics solver is also the portion that integrates the nonhydrostatic Euler equations forward in time with a time-split integration scheme, using user-specified grid, boundary layer, and initialization conditions (Skamarock et al., 2008). In essence, it is the ARW solver which makes the WRF customizable to each user and allows comparison between model runs with varying formulations to evaluate any model effects on forecast differences. Within the ARW solver, there are a variety of available physics schemes the user can incorporate, including the microphysics, cumulus convection, surface physics, planetary boundary layer physics and atmospheric radiation physics parameterizations. For this study, we are mostly interested in the effects of changing the microphysics parameterization, but the effect of using different

---

[1] https://www.mmm.ucar.edu

cumulus and planetary boundary layer parameterizations will be investigated as well in order to establish the sensitivity of the hemispheric waviness forecast to variation of each of these components of the parameterized physics. There is a relationship between all of these physical parameterization schemes, meaning altering one does have impacts on the others, and thus the resulting forecast. A schematic of the relationship between the various parameterizations is shown in Fig. 5.

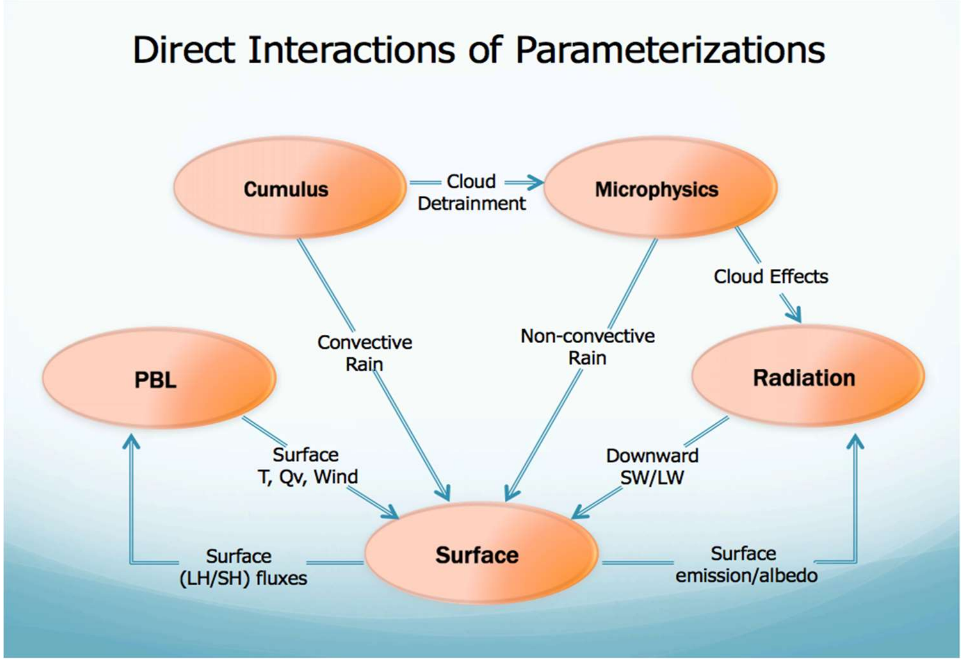

Figure 5: The relationship between the physical parameterizations in the WRF ARW model. From http://www2.mmm.ucar.edu/wrf/users/tutorial/tutorial_presentation_winter_2018.

3.2 Model Setup

The WRF ARW version 3.8 is the basis for all the model runs used in this study. The model domain encompasses the entire northern hemisphere in the east-to-west direction extends from 25° S to 85° N. The east-to-west boundaries are periodic, such that the data passed out the one end is received by the other to ensure continuity in the flow. The horizontal grid resolution is nominally 80 km. This coarse resolution was selected because we are mainly interested in the flow on the planetary- and large synoptic-scales, rather than in resolving mesoscale features. The model has 30 vertical terrain-following eta (η) levels, with the reference model top pressure being 50 hPa.

The WRF model was run every day from 01 November 2016 through 31 March 2017, defined as the cool season for this study. The model was initialized each day at 0000 UTC with updates at the boundary conditions provided every three hours using 0.5° GFS forecast data from the National Climate Data Center (NCDC). Before running the WRF, we selected four different microphysics schemes of interest to interchange over the course of the experiment. Unless otherwise specified, the remainder of the WRF initial settings and conditions remained identical, with the only difference between runs being the microphysical parameterizations in place. Once the specified microphysics scheme was in place, the WRF was run out for 120 hours.

To investigate the relative role of microphysics on the hemispheric sinuosity compared to that of other physics parameterizations, we also conducted experiments from simulations employing different planetary boundary layer (PBL) and cumulus (CU) schemes. The differences between the individual schemes selected within each physical parameterization - MP, PBL, and CU - will now be explained.

3.2.1 Microphysics (MP) Schemes

Within an NWP model, the microphysics explicitly resolve water vapor, cloud and precipitation processes. In the version of the WRF used in this study, the microphysics is calculated at the end of a time-step as an adjustment process, so no tendencies are provided. By carrying out these processes at the end of the model time-step, the final saturation balance is accurate for the updated temperature and moisture (Skamarock et al., 2008). The four different microphysics schemes used were: the Kessler scheme (Kessler, 1995), a single moment 3-class scheme (Hong et al., 2004), the Eta Ferrier scheme (Rogers et al., 2001) and a no latent heat release scheme. Each of these options will now be explained in more detail.

The Kessler scheme (which we will refer to as 1MP) is the simplest scheme that releases latent heat. The 1MP scheme only has liquid water hydrometeors and its associated processes throughout the entire model and thus includes rain, condensed cloud vapor and water vapor. The microphysical processes within this scheme are: the production, fall, and evaporation of rain, the accretion and autoconversion of cloud water, and the production of cloud water from condensation (Dudhia, 2018; Skamarock, 2008).

The single moment 3-class scheme (3MP) adds a bit of complexity by including ice processes above the freezing level in the atmosphere. Single-moment schemes predict the mass of a species, then derive the particle size distribution from fixed parameters, while double-moment schemes also predict the number concentration per species (Dudhia, 2018). There are three categories of hydrometers: vapor, cloud water/ice, and rain/snow. When the temperature is above freezing in the atmosphere, cloud water and rain occur, and when temperatures are below freezing, cloud ice and snow occur, but there exists no mixed-phase hydrometeors. Supercooled water and gradual melting rates are not present, so this scheme is efficient computationally for the inclusion of ice, but is lacking with regards to complex interactions between phases and processes.

The most complex scheme used in this experiment is the Eta Ferrier (5MP) scheme. This scheme includes water vapor and condensate (cloud water, rain), cloud ice, and precipitation ice (snow/graupel/sleet). The total condensate is calculated using the combination of all of the individual hydrometer fields, with the water vapor and total condensate being what is advected within the model. Mixed phase processes are considered at temperatures above -30˚C (Skamarock et al., 2008).

The final microphysics scheme used did not include any latent heat or cumulus parameterizations (NOLH). This was run to provide a baseline against which forecasts of waviness unaffected by latent heat release could be compared to those shaped by latent heat release distribution as prescribed by the various complexity of microphysics parameterizations. Figure 6 shows a cartoon illustration of the different microphysics schemes used in this experiment and the way each processes the water substance.

3.2.2 Planetary Boundary Layer (PBL) Schemes

The differences between PBL schemes arise from their treatments of boundary layer mixing, dissipation and mass flux parameterizations. The PBL schemes provide atmospheric tendencies of temperature, moisture, and horizontal momentum in the entire atmospheric column by determining the flux profiles in the well-mixed boundary layer and the stable layer. They vary in their processing of turbulence kinetic energy, mass flux, and mixing (Skamarock et al., 2008).

The Yonsei University (YSU) PBL scheme, which we will refer to as 1PBL, is based on Hong et al. (2006). The depth of the PBL in this scheme is effectively determined by the buoyancy profile, in which the top of the PBL is defined to be at the maximum entrainment layer. The second PBL scheme (2PBL), is the Mellor-Yamada-Janjic (MYJ) scheme (Janjic, 1994). The upper-limit of the boundary layer in this scheme depends on the turbulent kinetic

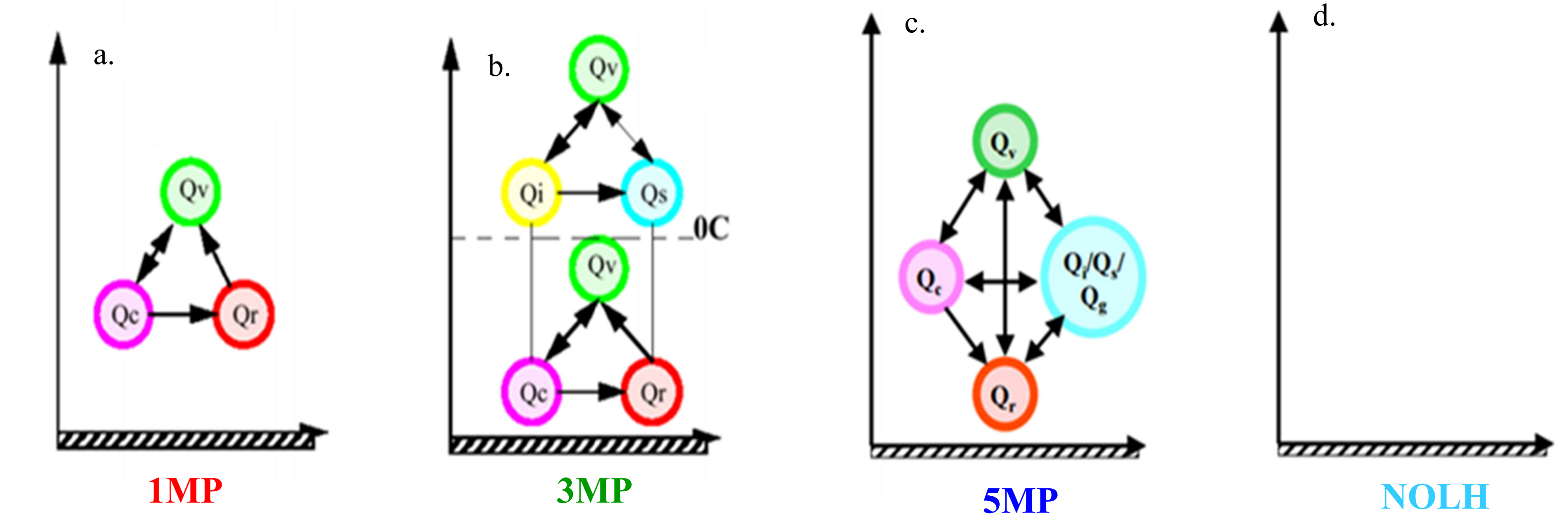

Figure 6: Cartoon of the different microphysics schemes used in the model: (a) The Kessler which will be referred to as 1MP; (b) The3-class scheme which will be referred to as 3MP; (c) The Ferrier scheme which will be referred to as 5MP; (d) The no latent heat scheme. The variables represent the latent heat of: condensation ($\mathbf{Q_c}$), vaporization ($\mathbf{Q_v}$), precipitation of rain ($\mathbf{Q_r}$), deposition ($\mathbf{Q_i}$), precipitation of snow ($\mathbf{Q_s}$), and precipitation of graupel ($\mathbf{Q_g}$).

energy and the buoyancy and shear of the driving flow. The final PBL scheme (7PBL) is the Asymmetric Convection Model 2 (ACM2) scheme (Pleim, 2007). Planetary boundary layer depth in this formulation is determined by the critical bulk Richardson number, which depends on absolute virtual temperature, virtual potential temperature difference across a layer, and the changes in the zonal and meridional wind components across the same layer (Skamarock et al., 2008).

3.2.3 Cumulus (CU) Schemes

The goal of the cumulus schemes is to parameterize the sub-grid-scale effects of convection and/or shallow clouds. The first cumulus scheme used is the Kain-Fritsch (KF) scheme, which we will refer to as 1CU (Kain, 2004). It uses a simple cloud model with moist updrafts and downdrafts, including detrainment and entrainment effects. In addition to cloud liquid and ice, rain and snow can also be detrained at cloud top. The second cumulus scheme (2CU) is the Betts-Miller-Janjic (BMJ) scheme (Janjic, 1994). There are no explicit updrafts or downdrafts, and no cloud detrainment. Instead of a mass flux method, this is the only scheme of the four used in this study in which the column undergoes moist adjustment, relaxing to a well-mixed profile. The Grell-Freitas ensemble scheme is the third cumulus scheme employed, and will be referred to as 3CU (Grell and Freitas, 2014). It uses an ensemble of triggers and closures to run multiple (up to 144) members each with varying parameters, in the grid box, then averages the result to get a value for each grid box. Clouds within each ensemble member can have different updraft and downdraft entrainment and detrainment parameters, including ice detrainment, as well as precipitation efficiencies (Dudhia, 2017). The final cumulus scheme, 4CU, is the old simplified Arakawa-Schubert

Scheme (SAS) (Pan and Wu, 1995). Deep and shallow (which can be enhanced by mixing) convection can occur, in addition to downdrafts in a single cloud. All of the schemes have no momentum tendencies and allow shallow and deep convection, but vary in their parameterization of updrafts, downdrafts, and cloud entrainment and detrainment, as well as when to trigger a convective column. The schemes detrain cloud rain and ice at the top of the cloud (except 2CU), which is then used by the microphysics scheme employed (Skamarock et al., 2008; Dudhia, 2017).

3.3 Sinuosity

A variety of jet waviness metrics have been introduced within the last decade. Previous studies use a zonal background state to calculate departures of geopotential height isopleths or isentropic PV contours (Francis and Vavrus, 2012, 2015; Screen and Simmonds, 2013a; Röthlisberger et al., 2016), while others isolate particular latitude bands and perform Fourier analysis on the meridional wind or geopotential height (Petoukhov et al., 2013, Coumu et al., 2014; Screen and Simmonds 2013a, 2014). In this paper, we utilize a new way of calculating the waviness by borrowing a concept from geomorphology: sinuosity. This method does not use long-term background states or a latitude band as a platform; rather it calculates the departure from zonality of the jet-level flow on a given day using only the 200 hPa heights.

In geomorphology, the sinuosity is defined as the ratio of the length of a stream segment to the length of the shortest distance between the endpoints of the segment (Leopold et al., 1964), as illustrated in Fig. 7. Taking advantage of the approximate geostrophic balance of the mid-latitude flow, this method can be applied to geopotential height contours of jet-level flow to provide a measure of the departure of zonality of the jet-level flow.

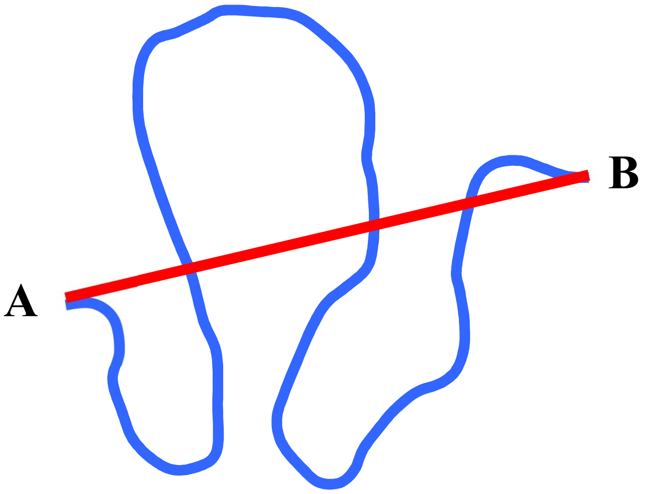

$$S_{AB} = \frac{\text{(Length of CONTOUR)}}{\text{(Length of SEGMENT)}}$$

Figure 7: Showing the curviliner length of a segment (blue) and the shortest distance between the two endpoints (red). S_{AB} denotes the equation for the sinuosity between the two points. Figure from Martin et al., 2016.

As an example, we selected one closed isohypse at 500 hPa, as shown in Fig. 8. This isohypse encloses a certain area and has a measurable length. Cut-off features of an isohypse (i.e. cut-off lows or highs) are included, as these features also have measurable lengths and areas, which can be easily added linearly into the calculation. The finite area

contained within the isohypse and any cut-offs is equal to that contained within a polar cap whose southern latitude is defined as its *equivalent latitude*. To calculate the sinuosity, we take the ratio of the length of the given isohypse to the length of its equivalent latitude circle.

A sinuosity of 1 would indicate that the flow is zonal, whereas the larger the value is above 1, the larger the departure from zonality at that given time.

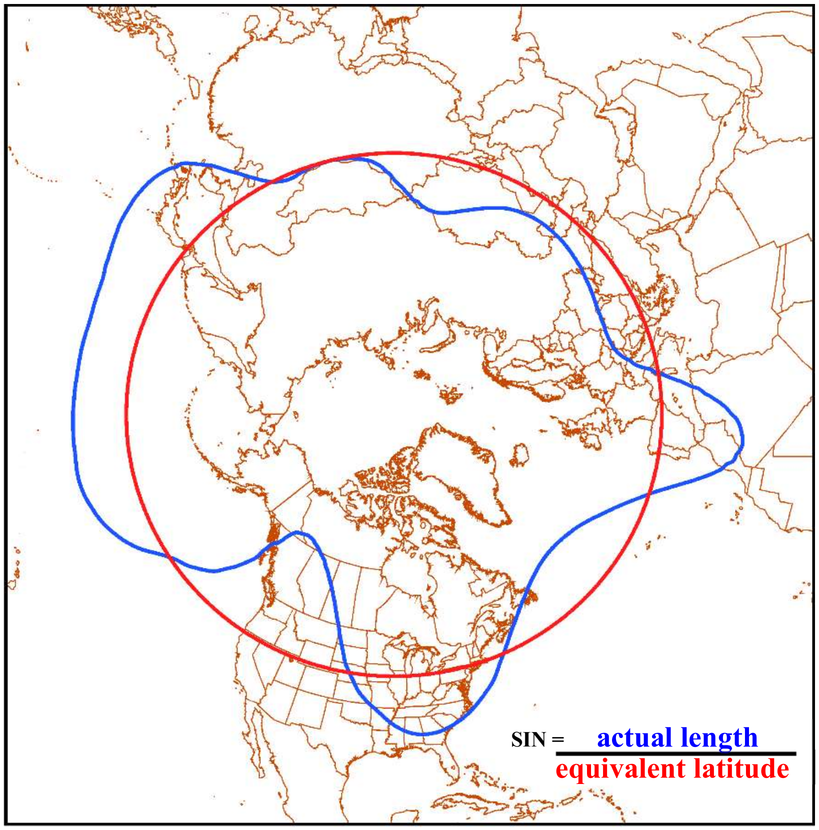

Figure 8: The actual length (blue) of the 552 decameter isohypse on 18 January 2014, and its equivalent latitude (red). Figure from Martin et al., 2016.

For all of the sinuosity calculations shown, we calculate the aggregate sinuosity of six isohypses (11250, 11430, 11610, 11790, 11970 and 12150 m) at 200 hPa bound by the latitudinal region of 10° - 80° N. This range of isohypse was selected because it approximately houses the tropopause-level jet during the cool season. The aggregate sinuosity at a given time is the ratio of the sum of the length of all six isohypses divided by the sum of the length of all six equivalent latitudes at the same time.

For the 66-year mean sinuosity calculation, we employ the NCEP/NCAR reanalysis data (Kalnay et al., 1996) four times daily for the 200 hPa data from 1 January 1948 to 28 February 2014 on a global 2.5° x 2.5° grid. To find the average, we use each calendar day's average sinuosity over the 66-year period. To calculate the observed sinuosity for the 2016-2017 cool season, we used the GFS initialization data described above, which is available four times daily on a 0.5° x 0.5° grid.

4. RESULTS

In order to identify unusually wavy or non-wavy events during the 2016-17 cold season, the 66-year daily average sinuosity for the November – March (NDJFM) period was calculated from the NCEP Reanalysis data. The following analysis is split into two broad categories. We first identify one maximum and one minimum sinuosity departure event of interest in the manner just described. Next, we evaluate the effects of changing the microphysics parameterizations on 120-hour forecasts of 200 hPa aggregate waviness for each event. These forecasts are compared to the observations valid at the same time, to evaluate how faithfully the different schemes represented the analyzed waviness throughout the forecast period. We also conduct experiments changing the planetary boundary layer and cumulus schemes while holding the microphysics schemes constant to evaluate their effects on the 120-hour forecast. Finally, we take the quantitative difference between each scheme's forecast sinuosity and the observed sinuosity at each forecast lead time throughout the entire 2016-17 cold season. This allowed us to determine how the accuracy, as measured by sinuosity, of each of the schemes changed throughout the 120-hour forecast, and if one scheme was consistently more or less accurate through the forecast period over which this study was conducted.

4.1 Long-Term Sinuosity

The 66-year daily average sinuosity for NDJFM is shown along with the daily time series from 2016-17 in Fig. 9. There is a clear seasonal cycle observed in the average sinuosity, with an annual minimum occurring in February, and a maximum (not shown) occurring in July. Of particular interest are the period of maximum and minimum

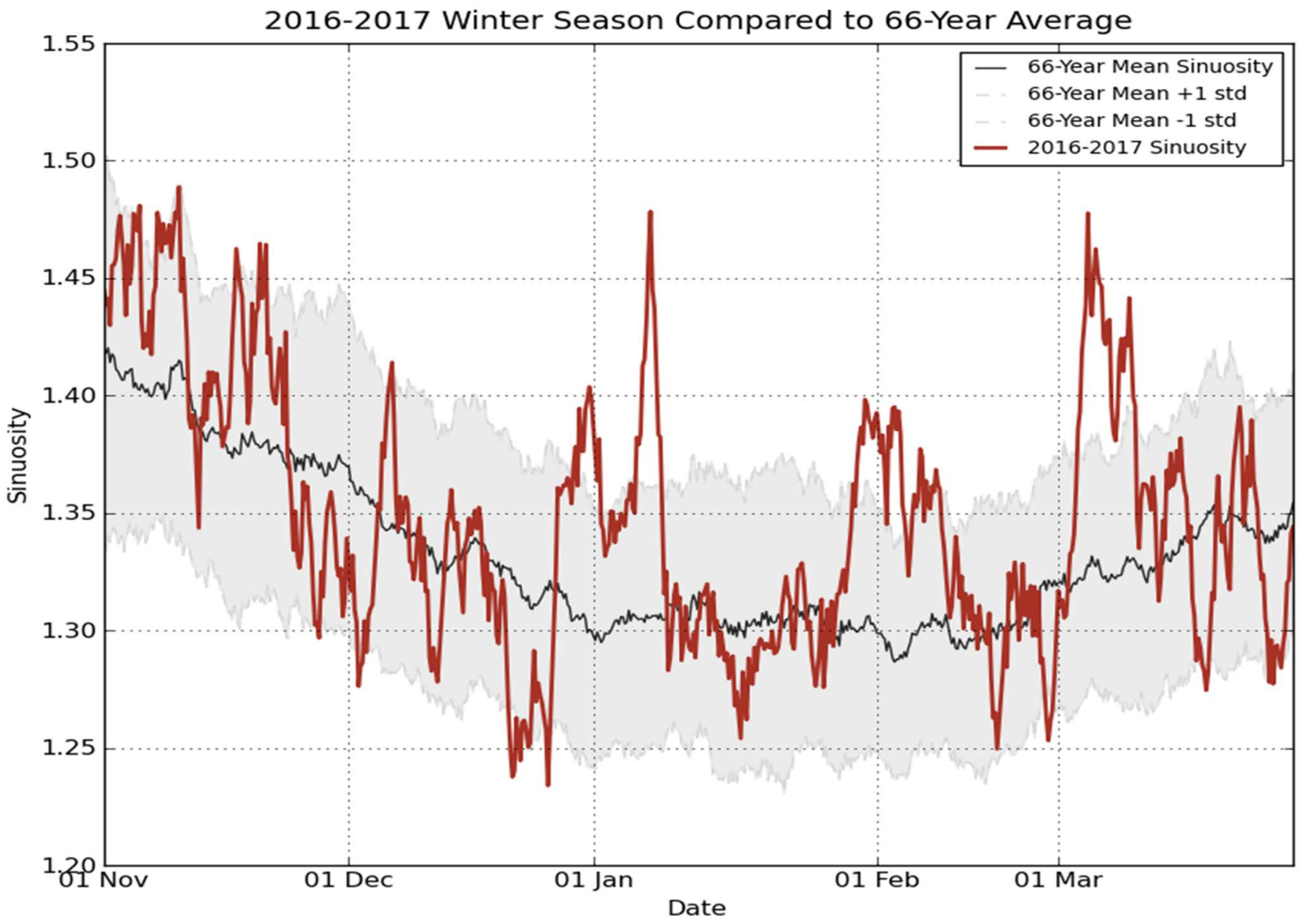

Figure 9: The 66-year mean sinuosity from 1 January 1948 to 28 February 2014 (black), and the +/- 1 standard deviation for the mean (grey shading), and the 2016-2017 observed sinuosity (red). 66-year mean (red). +/- 1 standard deviation regions are shaded grey, with the +/- 1 value marked with the black dashed line.

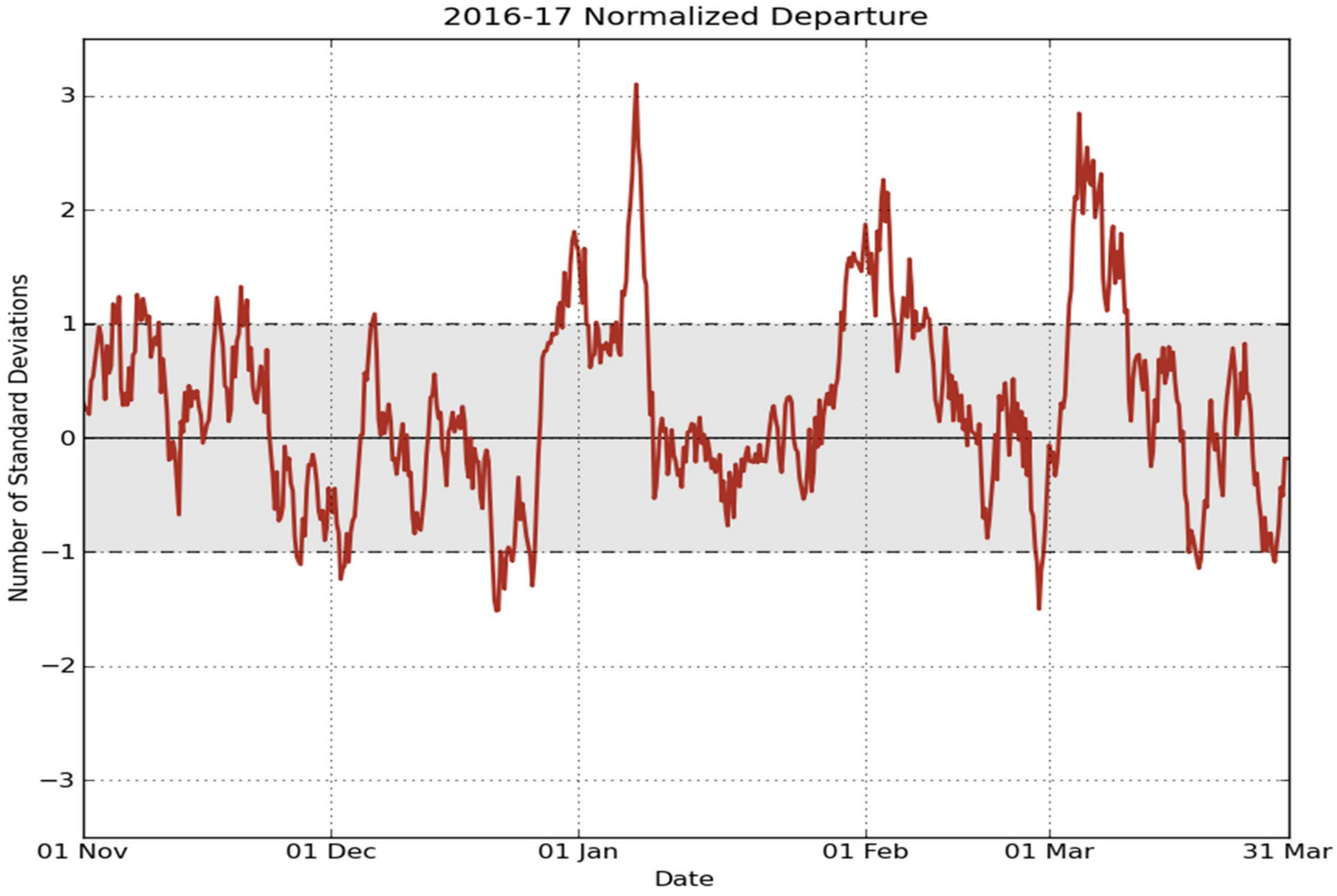

Figure 10: The normalized departure of the 2016-2017 sinuosity from the 66-year mean (red). +/- 1 standard deviation regions are shaded grey, with the +/- 1 value marked with the black dashed line.

sinuosity departure during the 2016-2017 season, such as the end of December, or the beginnings of January and March.

The same maxima and minima events stood out in the normalized departures for the results shown in Fig. 10. The remainder of this paper will focus on analysis of an anomalously high and anomalously low sinuosity event. The maximum sinuosity departure occurred on 08 January 2017 with a departure of 3.15 standard deviations above climatology, and minimum sinuosity departure occurred on 23 December 2016 with a departure of 1.51 standard deviations below climatology. The purpose of this comparison is to evaluate how accurately the different model microphysics schemes forecast high or low amplitude sinuosity events.

4.2 Maximum Sinuosity Event

A heavy rainfall event occurred on the west coast of the United States, particularly northern California, during the three days preceding 9 January 2017. An AR was located off the coast during this time and has been categorized as extreme on the Ralph/CW3E AR Strength Scale, indicating an integrated water vapor transport of > 1000 $kg\ m^{-1}s^{-1}$ (Ralph, et al., 2017). Between 6 and 9 January 2017, areas extending from central to northern California received over 12 inches of precipitation, causing flooding in lower elevations, with higher elevations observing heavy snow (Di Liberto, 2017). Figure 11a shows the location of the AR (circled) as it inundates the west coast of the United States, while Fig. 11b shows the radar estimated rainfall ending on 09 January 2017.

This AR, and the subsequent heavy flooding event was coincident with the observed maximum aggregate sinuosity departure for the 2016-2017 cold season. Both the AR and

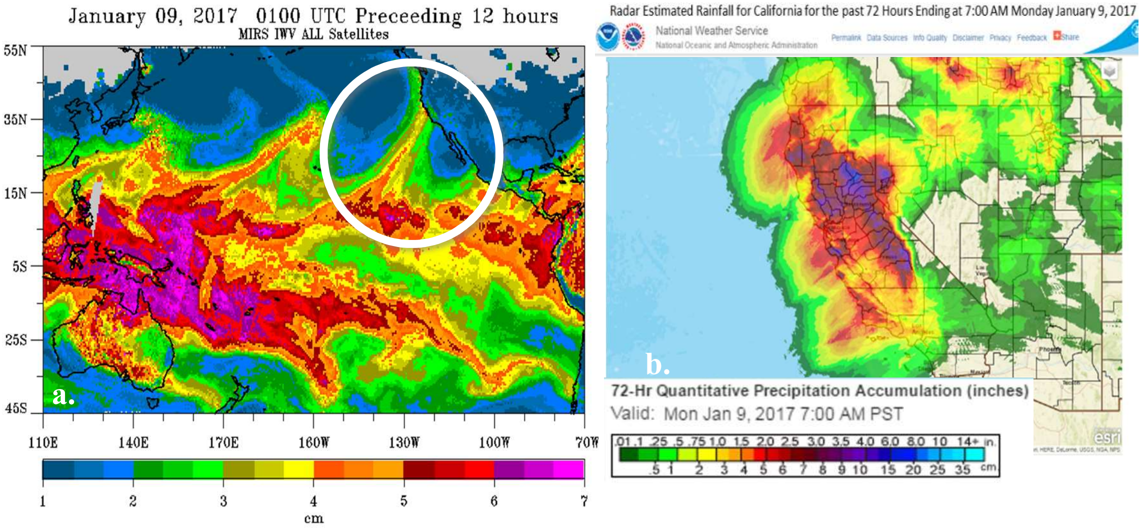

Figure 11: Left: Integrated water vapor valid 01 UTC and the preceding 12 hours on 09 January 2017. Image from http://www.esrl.noaa.gov. Right: Radar estimated precipitation from 15 UTC 6 January 2016 through 15 UTC 9 January 2017. Image from NWS Los Angeles/Oxnard.

aggregate sinuosity departure reached a maximum, in precipitable water intensity and normalized sinuosity departure, respectively, on 8 January 2017. To investigate this event, a WRF forecast was initialized at 0000 UTC on 5 January 2017. This puts the flooding and maximum AR intensity in the middle of the forecast period. The 200 hPa geopotential heights for the simulations employing of the varying microphysics schemes, at forecast hours F24, F72 and F120, are shown in Fig. 12. Note that throughout the analysis, we are not interested in amplitude and phase errors of each trough and ridge feature, but rather the *overall waviness* of the flow.

Figure 12a reveals that 24 hours into the forecast, a striking similarity exists among the four different forecasts of 200 hPa heights. The degree of similarity suggests that through the first day of simulation, the integrated effects of differences in the schemes are not sufficient to create a divergence in the forecast. By the end of three days of integration,

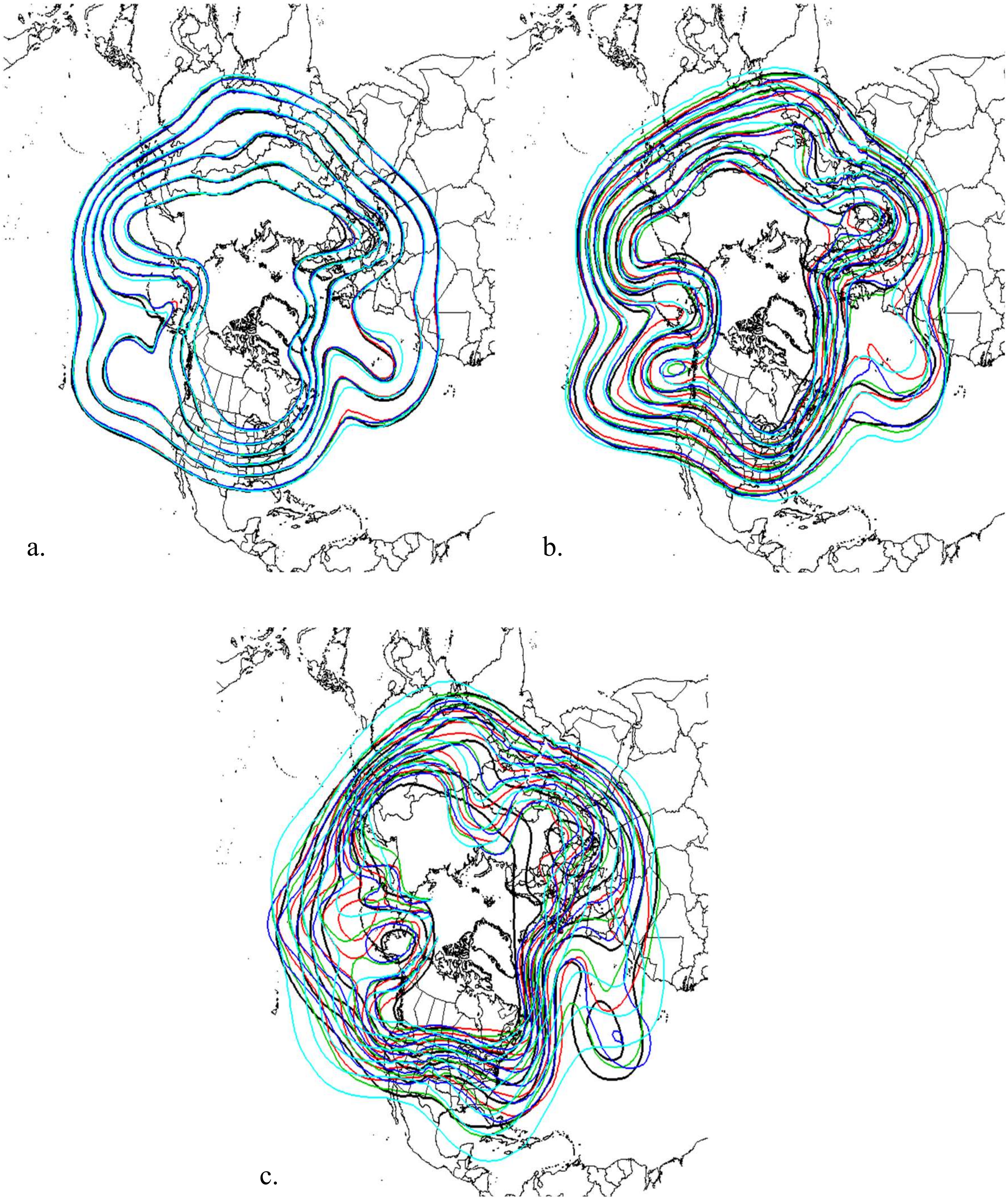

Figure 12: Forecast 200 hPa heights for varying microphysics schemes: 1MP (red), 3MP (green), 5MP (blue), and NOLH (cyan). Model initialized on 5 January 2017. Forecast times shown are: (a) 24-hrs, (b) 72-hrs, and (c) 120-hrs.

however, there are regions where the simulations exhibit differences, most notably over the eastern Atlantic (Fig. 12b). These differences become more dramatic and more widespread as the forecast length increases to 120-hours (Fig. 12c), where it becomes difficult to identify any regions over which the forecast heights are similar to one another, let alone which scheme is closest to the analysis valid at this time. In order to measure the differences amongst the simulations with respect to waviness of the flow and to compare them each to the waviness of the verifying analyses throughout the forecast period, we employ the aggregate sinuosity.

The aggregate sinuosity was calculated for each of the four forecasts, as well as the verifying analysis, beginning at the initialization time and throughout the entire 120-hr forecast. The results are plotted in Fig. 13. It is obvious that the aggregate sinuosity for each scheme, as well as the magnitude of differences between the schemes, changes through the forecast period. After forecast hour 36 the schemes start to diverge from one another and from the analysis, with the 3MP scheme increasing the sinuosity at a rate that closely follows the analysis, while the 1MP and 5MP schemes increase the sinuosity at a faster rate reaching a slightly higher maximum value and at an earlier time. The NOLH scheme consistently produces a less wavy flow than both the analyses and the other schemes. This result provides additional evidence of the importance of latent heat release on modulating the waviness of the upper-level flow. During the final 36 hours of the forecast, both the 1MP and 5MP scheme produce their maximum waviness while the 3MP scheme is notably less wavy than the analysis during this portion of the forecast.

To investigate the relative role of microphysics on the hemispheric sinuosity

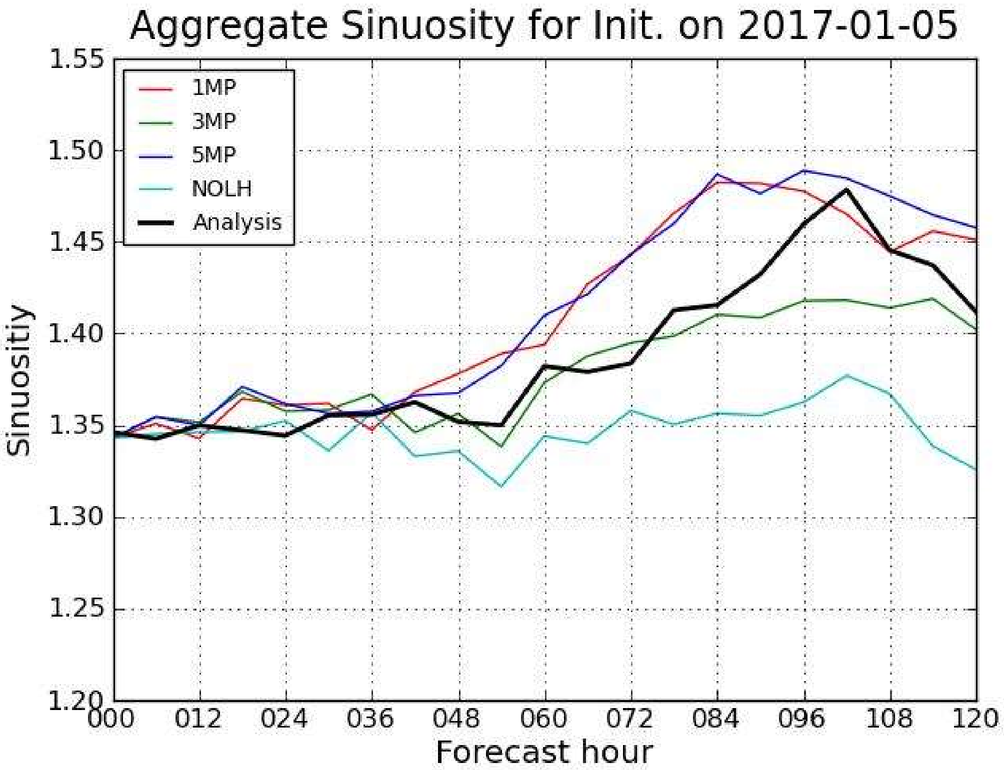

Figure 13: Aggregate sinuosity calculated using the 11250-12150m isohypses by 80m increments for WRF initialization at 00z on 5 January 2017.

compared to that of other physics parameterizations, we also calculated the aggregate sinuosity from simulations employing different boundary layer schemes. For this set of experiments, we maintained the 3MP scheme for all model runs. Figure 14a shows the results through the forecast period from using the different PBL schemes within the WRF. Comparison of this time series to that shown Fig. 13 demonstrates that varying the microphysics schemes leads to much larger spread in the aggregate hemispheric waviness at 200 hPa than varying the boundary layer schemes.

We ran a similar experiment to assess the influence of cumulus parametrizations on forecasts of aggregate waviness. Again, all CU schemes were used while retaining the 3MP

Aggregate Sinuosity with 3MP for Changing PBL Schemes

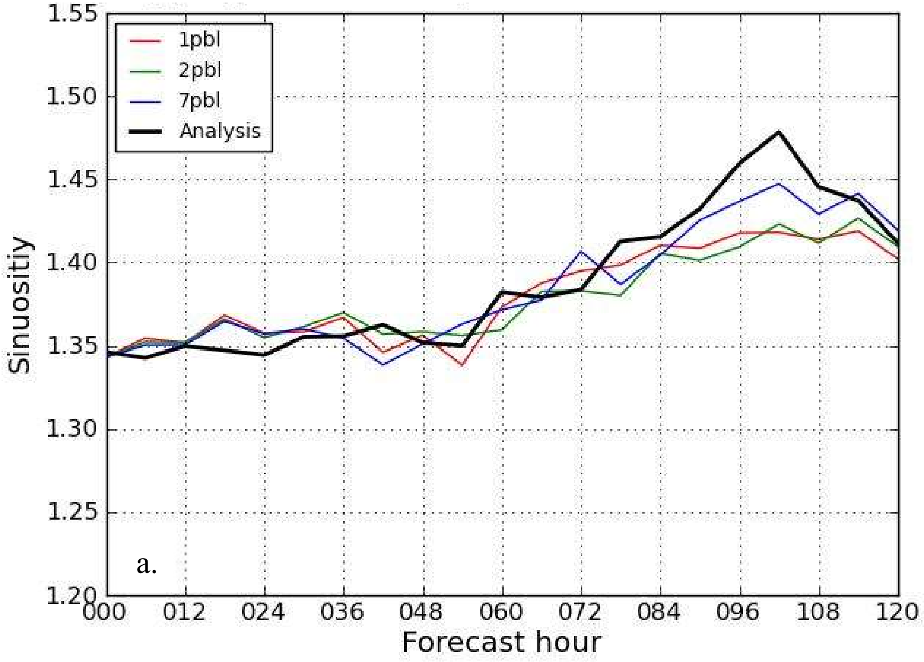

Aggregate Sinuosity with 3MP for Changing CU Schemes

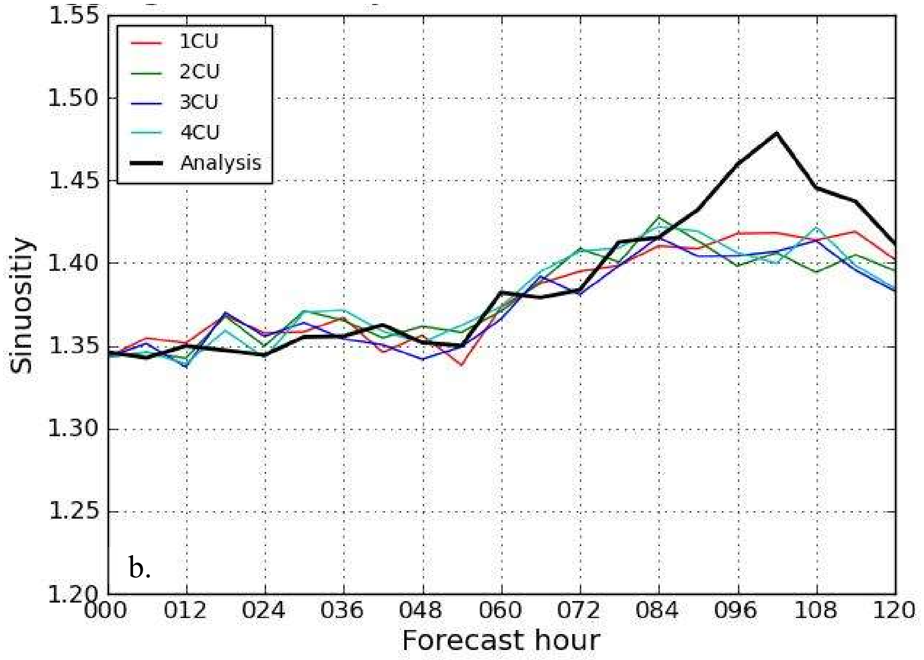

Figure 14: Aggregate sinuosity results from changing the (a) boundary layer scheme and (b) the cumulus scheme within the WRF. All model runs maintained the 3MP scheme.

through all the changes to the cumulus schemes. Figure 14b shows that a much smaller spread in the aggregate sinuosity forecast across the hemisphere results from changing the cumulus schemes as compared to changing the microphysics parameterizations (Fig. 13). In fact, it appears that the forecast waviness associated with the various cumulus schemes in Fig. 14b follows the shape of the 3MP line observed in Fig. 13. This led us to conduct further experiments designed to evaluate the nature of the influence of various combinations of microphysics and cumulus parameterizations.

Figure 15 shows a matrix of possibilities over which we can examine this question. For this study, we are only interested in comparing simulations across the rows of this matrix. That is, we will be assessing how changing the cumulus scheme across fixed microphysics packages affects the forecast waviness.

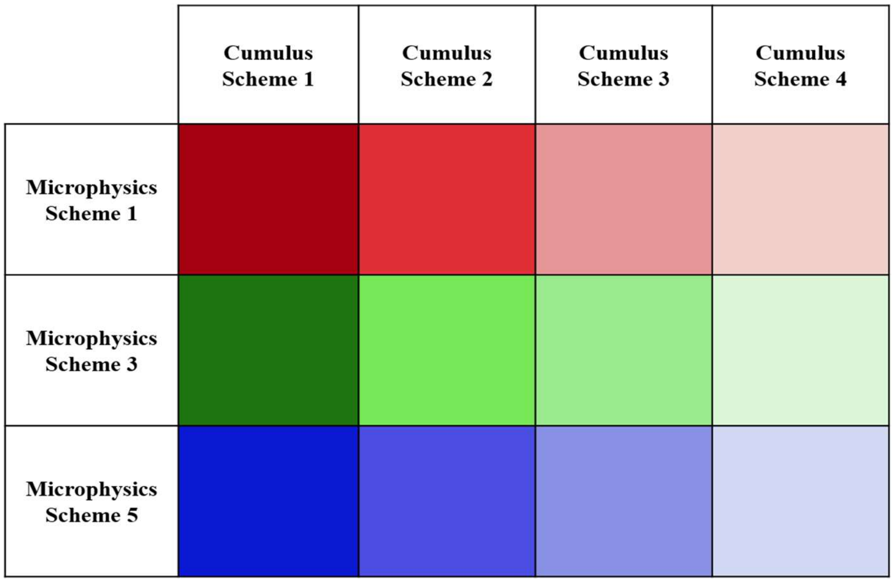

	Cumulus Scheme 1	**Cumulus Scheme 2**	**Cumulus Scheme 3**	**Cumulus Scheme 4**
Microphysics Scheme 1	🟥	🟥	🟥	🟥
Microphysics Scheme 3	🟩	🟩	🟩	🟩
Microphysics Scheme 5	🟦	🟦	🟦	🟦

Figure 15: A 3x4 matrix showing the possible combination of MP and CU WRF runs. In the experiment of changing the cumulus parameterization while keeping the microphysics scheme constant, we are interested in going across the rows of this matrix.

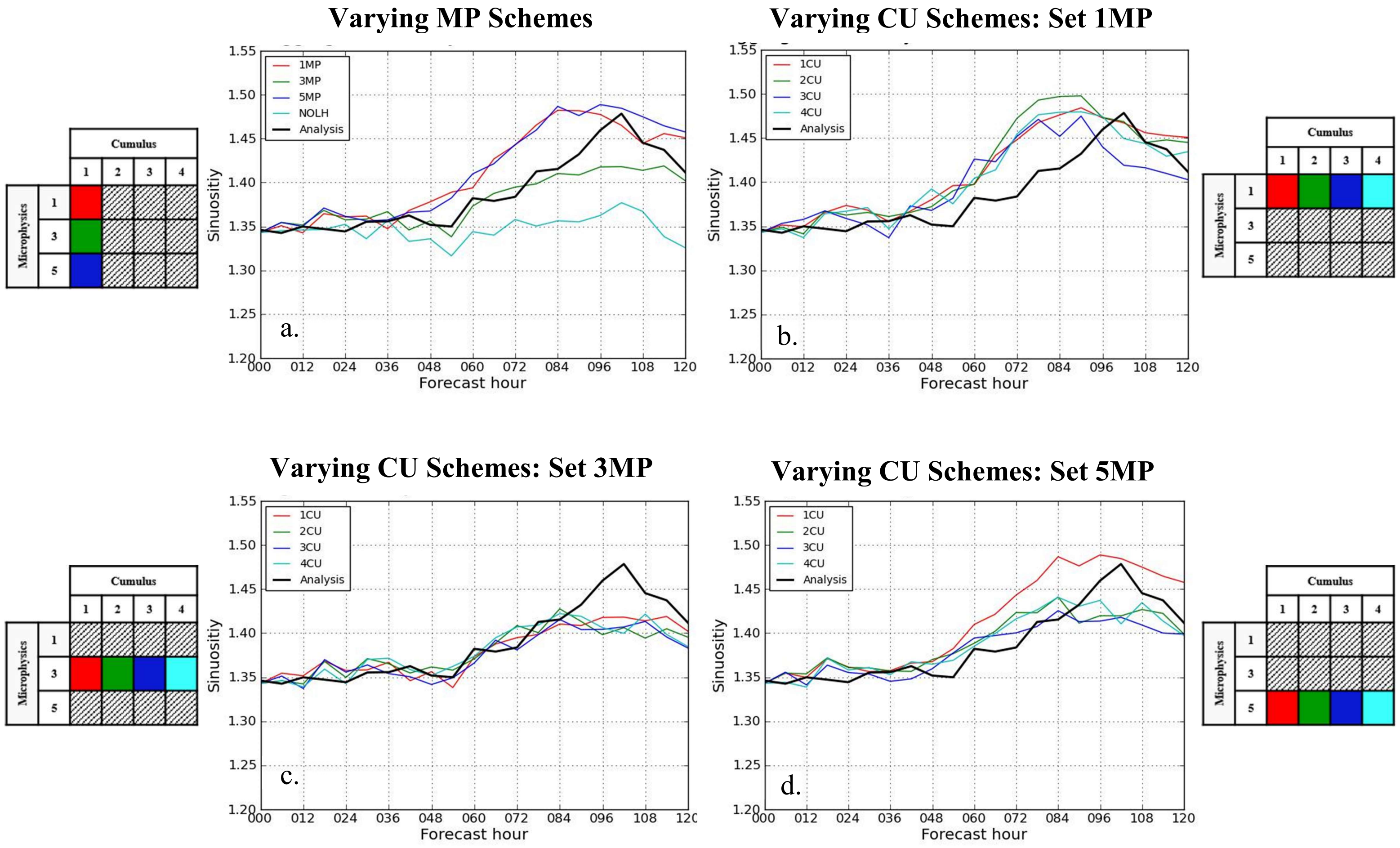

Figure 16: Aggregate sinuosity calculated using the 11250-12150 m isohypses by 80m increments for WRF initialization at 00z on 5 January 2017. (a) Fig. 13 repeated for easy reference and comparison. Effects of changing cumulus schemes across fixed microphysics schemes: (b) 1MP, (c) 3MP, and (d) 5MP.

Figure 16a (identical to Fig. 13), is repeated here to facilitate a set of insightful comparisons. The time series of aggregate sinuosity from a set of four experiments run by varying the cumulus schemes while holding the microphysics parameters constant at 1MP are shown in Fig. 16b. All four of the lines in Fig. 16b mimic the overall shape of the 1MP sinuosity shown in Fig. 16a. Holding the microphysics constant at 3MP across the four cumulus parameterizations (Fig. 16c) likewise results in four time series that mimic the 3MP time series in Fig. 16a. Holding 5MP constant throughout a similar set of simulations, however, does not produce a set similar to the 5MP time series in Fig. 16a. In fact, only the 1CU/5MP simulation looks like the 5MP time series shown in Fig. 16a. The other three look much more like the 3MP time series in Fig. 16a. The physical/computational reason for these discrepancies are not yet understood. Overall, these results hint at the possibility that choice in microphysics scheme impacts the downstream aggregate waviness of the 200 hPa flow in a more substantial manner than the cumulus scheme.

4.3 Minimum Sinuosity Event

The season's minimum sinuosity event occurred on 23 December 2016. During this time the jet was fairly zonal across Asia and Europe with few even moderately wavy features present across the hemisphere, as shown in Fig. 17. To analyze this event, we will use the WRF initialized at 00z on 20 December 2016. This puts the hemispheric minimum in aggregate sinuosity in the mid-range of the 5-day forecast, thereby mimicking the approaches used in our examination of the maximum sinuosity event.

Just as in Fig. 13, Fig. 18 shows the aggregate sinuosity across the 120-hour forecast for the four microphysics schemes, initialized on 20 December 2016. Through

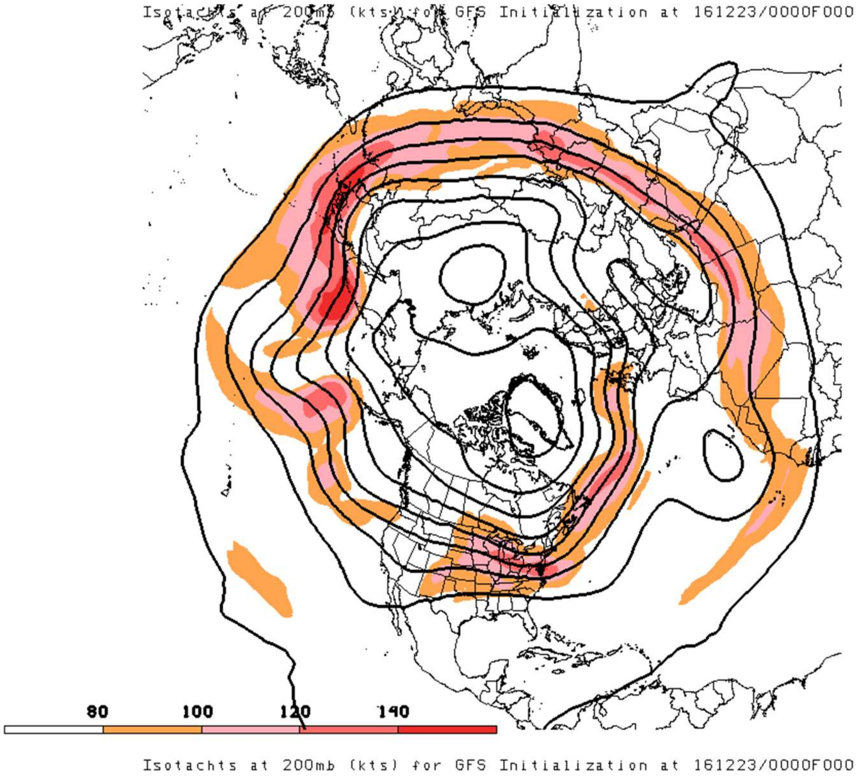

Figure 17: 200 hPa heights valid 23 December 2016. Shading indicates isotachs (knots) at 200 hPa beginning at 80 knots.

approximately hour 60, the three schemes with latent heat release, 1MP, 3MP and 5MP are all showing fairly consistent values of aggregate sinuosity, not only between the members but compared to the analysis as well. This is different from Fig. 13, which exhibited such similarity between members only through approximately 36 hours. The notable increase in forecast accuracy for longer lead times during an episode of diminished waviness may be a result of the presumed decrease in storminess that might reasonably be expected in such a hemispheric flow. Fewer storms would presumably correspond to less latent heat release and thus, since microphysics parameterizations are mobilized in regions of latent heat release, their relatively less active role in shaping the flow during a period of decreased waviness might account for the small spread between the schemes and the analysis persisting longer into the forecast.

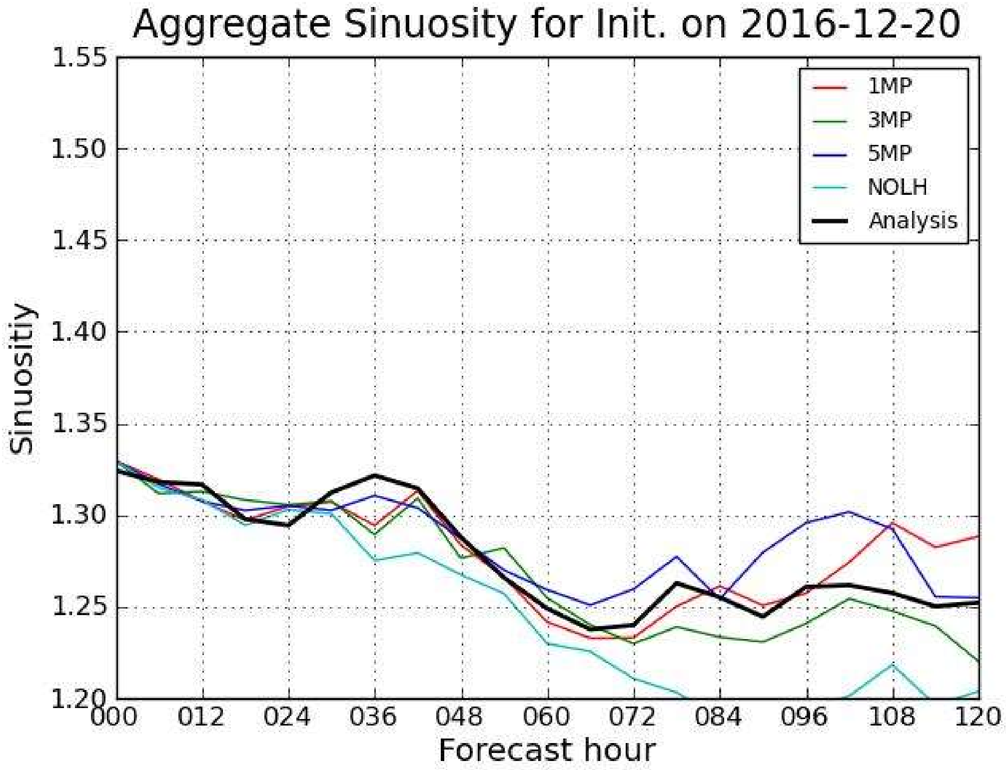

Figure 18: Same as Fig. 13 but for initialization on 20 December 2016

After the first 60 hours, the four schemes and analysis start to diverge, while the no latent heat package produces a consistently and significantly less sinuous flow than the other schemes and the analysis. There is a similar pattern observed in Fig. 18 as there is in Fig. 13: the 3MP scheme produces less sinuosity than the 1MP and 5MP schemes. This tendency is notable throughout the entirety of the cold season (not shown). In addition to having a longer period during which the schemes have similar sinuosity values (60 hours *vs*. 36 hours), the forecast for the minimum sinuosity event also has a smaller spread between the microphysics members compared to the maximum sinuosity event, as well as smaller spread between the members and the analysis. This illustrates that there is less forecast error and uncertainty relative to the analysis for the forecasts initialized on 20 December 2016 (the minimum sinuosity event) than there is for the forecasts initialized on 05 January 2017 (the maximum sinuosity event). This will be explored further in the next section in which the seasonal sinuosity results are discussed. Because, by construction, sinuosity cannot be less than 1.0, the reduced spread amongst the various schemes is at least partially a function of the close approach to this limiting value for a minimum sinuosity event.

We again investigated the effects of changing the planetary boundary layer and cumulus parameterizations for the same minimum waviness forecast period to evaluate the impacts. For this experiment, the 3MP scheme was again held constant between the runs, so the only changes made were to the boundary layer or cumulus schemes. Figure 19a shows a much smaller spread in the forecast aggregate sinuosity through the 120-hour period arises from varying the boundary layer parameterizations as compared to the microphysics parameterizations (Fig. 18).

Curiously, we again noted that when varying cumulus schemes (Fig. 19b) while holding the 3MP scheme constant, these forecasts seemed to follow the spine of the 3MP scheme (Fig. 18). To assess the impact of varying cumulus parameterizations across a set of fixed microphysics parameterizations for the minimum sinuosity event, we recreated the four-panel analysis for the maximum sinuosity event (and shown in Fig. 16) for the minimum sinuosity event.

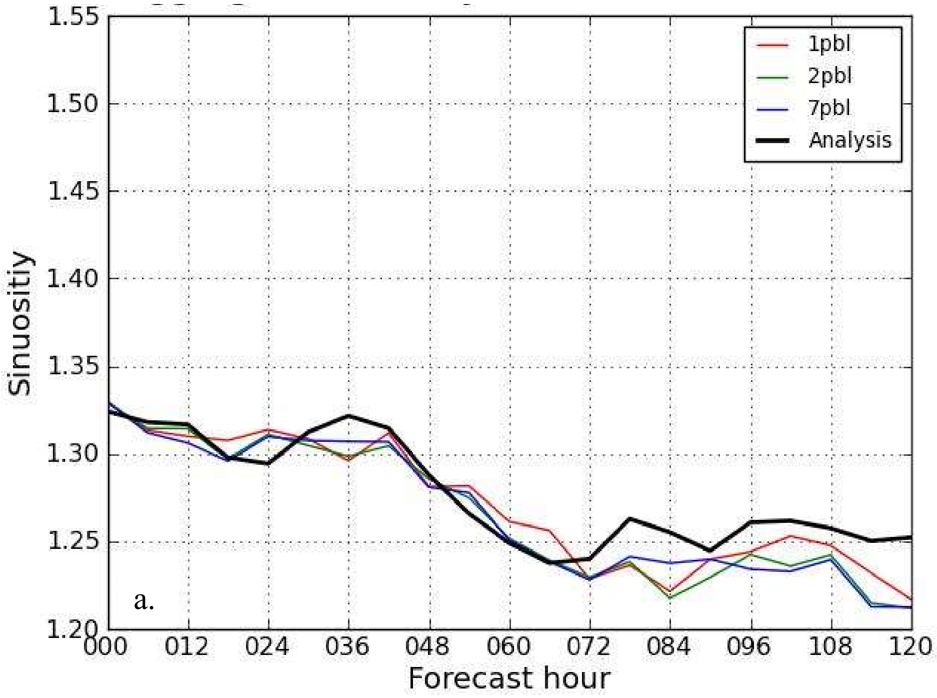

Aggregate Sinuosity with 3MP for Changing PBL Schemes

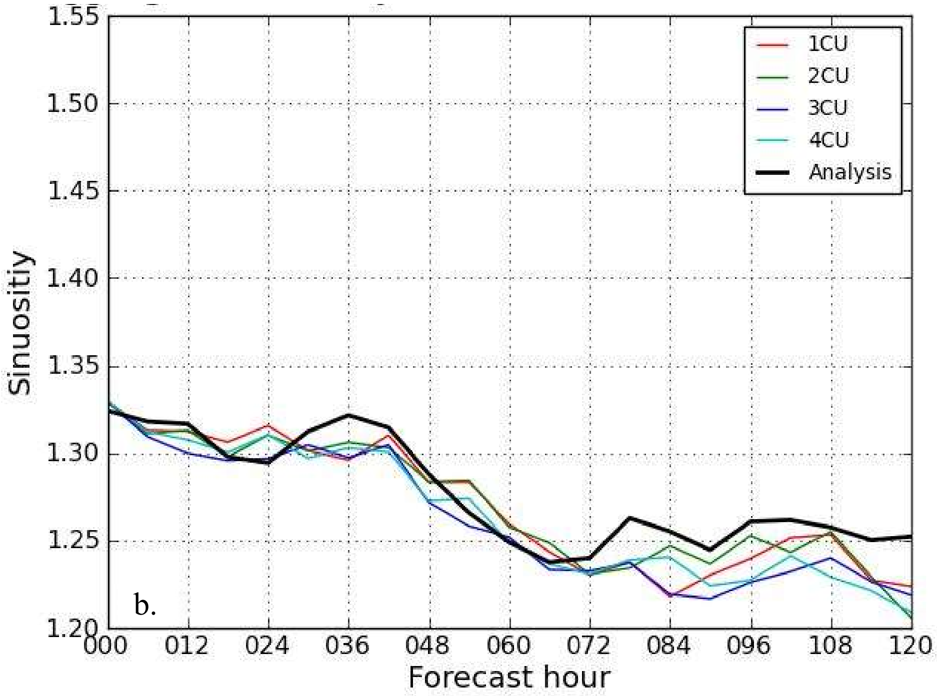

Aggregate Sinuosity with 3MP for Changing CU Schemes

Figure 19: Same as Fig. 14 but for initialization on 20 December 2016.

The shape of all four lines in Fig. 20b, constructed from forecasts with variable cumulus parameterizations but a fixed 1MP scheme, conform to the overall shape of the 1MP line in Fig. 20a. An analogous fidelity to the original 3MP time series (Fig. 20a) results from varying the cumulus parameterizations across a fixed 3MP scheme (Fig. 20c). Figure 20d shows the experiments run holding the 5MP package constant across the cumulus schemes follow a similar shape as the original 5MP in Fig. 20a; however only through the first half of the forecast. After forecast hour 60, the magnitude of the forecast sinuosity values for the 2CU, 3CU, and 4CU schemes, do not match as well to the 5MP values shown in Fig. 20a, and after 84 hours into the forecast, there is no resemblance in magnitude or shape to the original 5MP line.

The results of this set of experiments run on the extremes of sinuosity from this cold season suggest that medium-range forecasts of jet-level hemispheric waviness are more strongly influenced by choice of microphysical parameterization than by any of the other leading physical parameterizations commonly employed in numerical models.

4.4 Seasonal Sinuosity Spread

In addition to monitoring how the spread among the different schemes increased with longer forecast lead-time, we were also interested in the average difference of the forecasts from analyses for each microphysics scheme. For each forecast made with each scheme there is a measurable difference between the forecast sinuosity and the analysis sinuosity at each of the 20 selected forecast times. These differences measure how accurate each scheme was at every forecast time. To calculate this difference for each microphysics scheme across the cool season, we first separated the data by scheme. Next, the difference calculation was

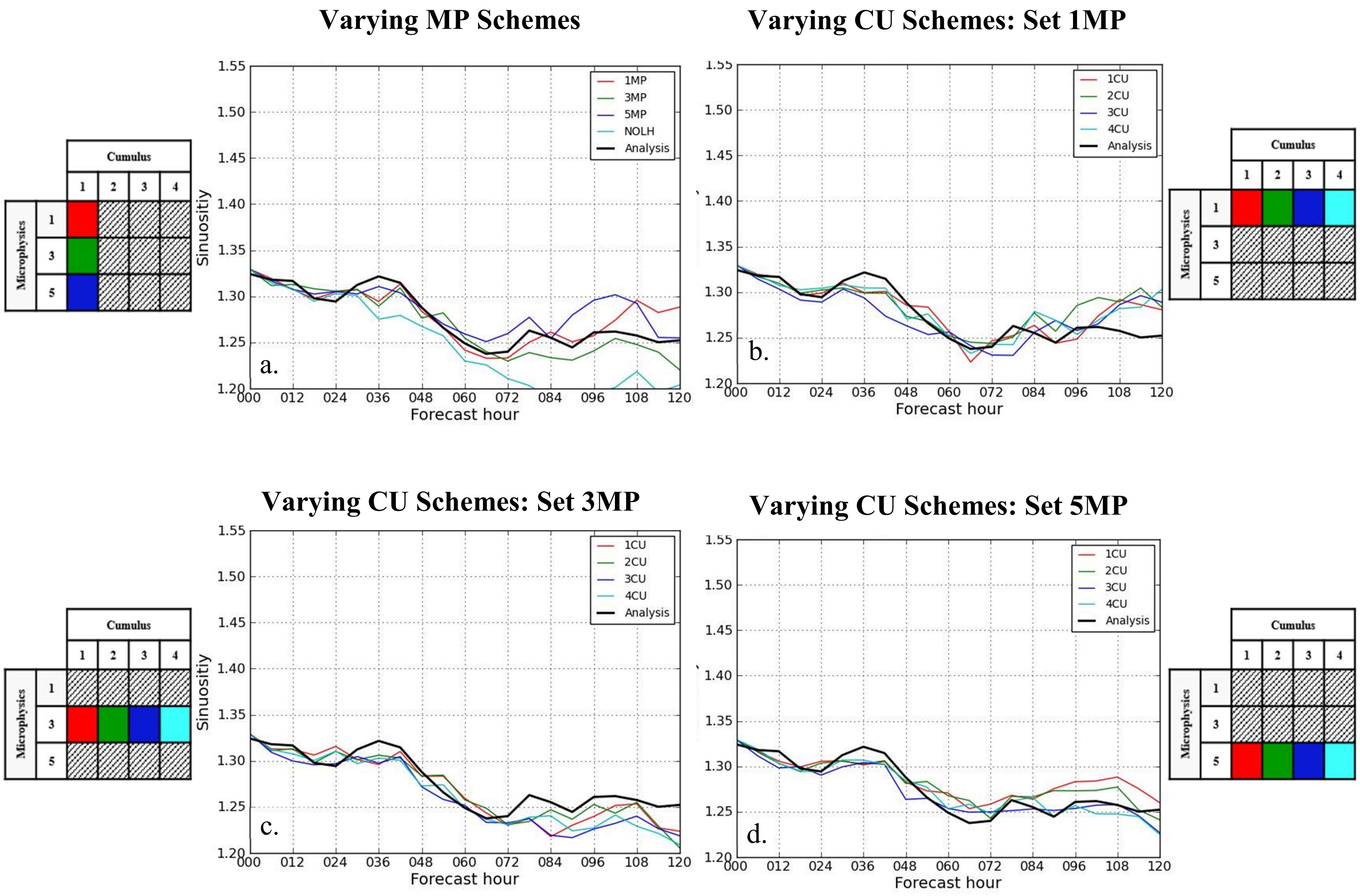

Figure 20: Same as Fig. 16 but for initialization on 20 December 2016.

defined as the absolute value of the forecast sinuosity value minus the analyses sinuosity value at every forecast hour for every day in the 151-day period, across all three of the microphysics schemes. Only absolute values were used to characterize the magnitude of the difference because the schemes could be more or less wavy than the analysis, resulting in a positive or negative value for the difference, respectively. Finally, we created box and whisker plots to show how differences in the accuracy of forecasts of sinuosity changed over the 5-day forecast period. By plotting this difference through the season, we are able to see, for example, if one scheme was consistently more accurate in forecasting the sinuosity value through a certain point in the forecast, or if one scheme had systematically less error in its forecast of sinuosity. In addition, by comparing the spread across the schemes we can determine if one scheme was consistently better in forecasting the sinuosity through a portion of the entire the 5-day period.

The results of this analysis are shown in Fig. 21. In addition to percentiles as indicated by the boxes in Fig. 21, we were also curious how the mean difference between the scheme and the analysis evolved through the forecast period. That average difference is plotted as the solid line through each of the plots. Both the vertical length of the blue boxes, as well as the whiskers on their ends, testify to the fact that the average difference between forecasts and analyses increases with increasing forecast hour. While all three schemes demonstrate such an increase throughout the forecast period, forecasts using the 3MP scheme (Fig. 21b) are clearly the least divergent. These cold season average results are consistent with the analyses of the maximum and minimum sinuosity events presented

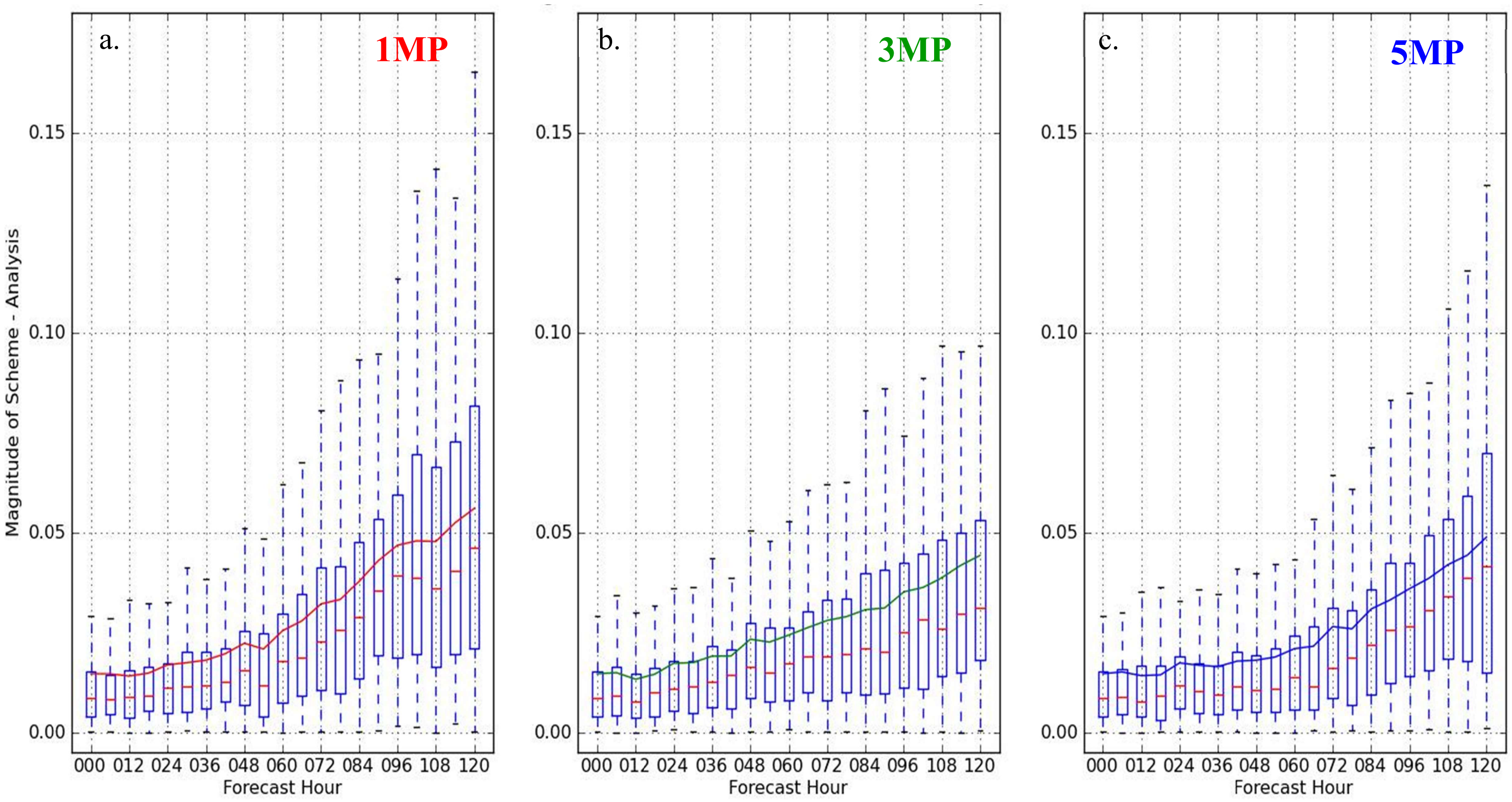

Figure 21: Boxplots of the difference between forecast aggregate sinuosity and the aggregate sinuosity of the analysis for each 6-hour forecast period in the 120-hour forecasts. Blue boxes bound the 25th and 75th percentiles, the red lines within the boxes indicate the 50th percentile, and the dashed lines below and above show the 0th and 100th percentiles, respectively. The solid colored lines through the boxes indicate the mean value of the difference magnitude: (a) for the 1MP, (b) for the 3MP and (c) for the 5MP scheme.

earlier; that is, the 3MP scheme's forecasts of 200 hPa aggregate sinuosity most faithfully reproduced the analysis through the forecast period.

Looking at how the mean difference magnitude changes through the forecast between each scheme, again we see that the 3MP has the lowest mean difference magnitude between the forecast and analysis at hour 120. It is also interesting to note that at the end of the forecast period, the 1MP scheme has the largest average forecast difference magnitude. The most complex 5MP scheme was the middling performer, registering an average error value nearly precisely in-between the best and worst performing schemes at the final forecast hour.

5. SUMMARY

This thesis describes the impact that the choice of microphysics parameterization within the WRF model has on hemispheric forecasts of the aggregate sinuosity of the 200 hPa flow. The potential downstream impacts of parametrizing microphysics processes were presented. Recent research shows that forecast errors, including the location and amplitude of Rossby wave breaking, PV streamers, cutoff lows, atmospheric rivers and warm conveyor belts, often result when considerable amounts of latent heat release characterize the flows to be simulated by NWP models. Recent studies have shown the impacts of these processes on specific downstream events, but have not considered the fundamental question of what impact the user's choice in microphysics parameterization might have on the overall hemispheric waviness.

For each day during the 2016-17 cold season (November – March), we ran four simulations using the WRF-ARW model each characterized by a different choice of microphysics parameterization. These microphysics schemes varied in complexity from no latent heat or cumulus parameterizations (NOLH), to warm rain processes (1MP) (Kessler, 1995), to liquid rain above 0˚C and ice processes below (3MP) (Hong et al., 2004), and finally to the cloud diagnostic variables including graupel and supercooled water (5MP) (Rogers et al., 2001). The waviness of the 200 hPa flow was calculated using a new method, sinuosity, borrowed from geomorphology. Sinuosity values range from a minimum of 1 (which indicates perfectly zonal flow), to larger values describing increasing departure from zonality for the flow. The aggregate 200 hPa sinuosity was calculated for each of the four daily simulations (out to 120 hours) for each day during the 2016-17 cold season. A maximum and minimum sinuosity event from that single season were identified and analyzed.

The maximum sinuosity event occurred on 08 January 2017 and was coincident with an AR that was associated with heavy rainfall along the west coast of the US. Looking at the four-different microphysics parameterization's 200 hPa aggregate sinuosity forecast through the 5-day forecast initialized on 05 January 2017, increasing spread between the individual different microphysics schemes, as well as between the forecasts and the analysis was observed with increasing forecast length. The 3MP scheme produced a forecast most faithful to the analysis, increasing sinuosity at a rate similar to what was observed, while the 1MP and 5MP schemes were wavier than the analysis. For the maximum sinuosity event, the divergence between the forecasts and analyses occurred at around 36 hours in the forecast. In order to assess the relative influence of the MP and CU schemes on forecast waviness, simulations in which pairs of parameterizations were varied were also run. Changing the cumulus schemes while keeping microphysics parameterization fixed produced forecast sinuosities with comparatively little variance around the control forecast with the microphysics scheme, particularly for the 1MP and 3MP schemes. For the cumulus parameterization simulations run while holding 5MP fixed, the forecast sinuosities were similar to the control for the first 36 hours of the simulation and noticeably diverged thereafter.

The minimum sinuosity event occurred on 23 December 2016, characterized by a minimally wavy jet around the hemisphere. WRF forecasts initialized on 20 December were used to analyze the event. Divergence between the four forecasts and the analysis sinuosity in this case appeared later in the forecast as compared to the maximum sinuosity event. It is suggested that this delayed divergence is a result of decreased storminess associated with a less wavy jet and, consequently, less influence of latent heat release on the evolution of the flow. Much like the maximum sinuosity event, changing the cumulus parameterization while holding the microphysics schemes constant resulted in forecast sinuosities that mimicked the control forecasts for the associated microphysical parameterizations, most notably for the 1MP and 3MP schemes. Varying cumulus parameterizations against a set 5MP scheme again resulted in a set of forecasts that exhibited low variance relative to the 5MP control forecast for only a limited portion of the 120-hour forecast.

The magnitude of the difference between each scheme's forecast and the analysis at each forecast time was calculated across the entire cold season and presented in a box and whisker plot analysis. It was found that differences between the forecasts of aggregate sinuosity and the analyses increased with forecast lead time. In addition, when calculated over the entire cold season, the mean difference between the forecast and the analyses at individual forecasts hours was smallest for the 3MP scheme through the length of the 120-hour forecast, and largest for the 1MP. This corroborates the broad result of the case study analyses (Fig. 13 and Fig. 18) namely, that the 3MP scheme is most similar to the analysis through the forecast period.

Accurately simulating and understanding the complex interactions, physical processes and diabatic heating at the microscale level is important for the reduction of downstream forecast errors in Rossby wave magnitude and location. By reducing these downstream errors, forecasts of high-impact sensible weather events, such as blocking, wave breaking and ARs can improve. The experiments conducted in this study suggest that the simulation of cloud microphysical processes, as parameterized in schemes of varying complexity, exerts a substantial control on forecasts of waviness in the jet-level flow.

5.1 FUTURE WORK

To gain more insight into the forecast sinuosity errors made by each scheme, a box-and-whisker plot showing the observed error (versus the magnitude of the error calculated by taking the absolute value of the observed error, as shown in Fig. 21) could be created. By looking at the observed error, model biases such as periods within each scheme where the model may under- or over-produce sinuosity on average can emerge. This would also provide insight into the skewness of the distribution, allowing an analysis on whether the larger errors associated with each scheme tend to be positive or negative. Such analysis could also be helpful in determining the source of the most extreme sinuosity forecast errors.

There are a variety of options when considering what work can be done in relation to this research question and methods used in this study in the future. First, it would be interesting to improve the model resolution to a finer grid spacing to see how the forecast sinuosity is impacted. It is possible that with a finer grid scale, smaller-scale features embedded in the flow can be resolved with more accuracy, thus leading to an impact on the forecast sinuosity. Second, I would like to compare forecasts of waviness over limited regions across the hemisphere and compare them to the values observed across the entire hemisphere. Recent studies, such as that by Röthlisberger et al. (2016), show that the genesis of waviness in localized regions can impact the waviness over the entire hemisphere. I would be interested to find out if there is a stronger signal of altered waviness in close proximity to high latent heat release events, versus further downstream, or if perhaps there is a correlation between high latent heat release in one sector to high amplitude flow in another. Finally, expansion of this work to other cool seasons would allow evaluation of other maximum and minimum sinuosity events. There are likely relationships between storminess, poleward moisture transport, and not only the forecast sinuosity, but also predictability of the sinuosity. Examining these relationships in closer detail could provide valuable insight into how forecasts involving high latent heat release events can be compromised and, eventually, be used to guide further improvements to model parameterizations.

REFERENCES

American Meteorological Society Glossary of Meteorology, 2017. Online. Retrieved from http://glossary.ametsoc.org/wiki/Main_Page.

Chagnon, J. M., S. L. Gray, and J. Methven, 2013: Diabatic processes in modifying potential vorticity in a North Atlantic cyclone. *Q. J. R. Meteorol. Soc.*, **139**, 1270-1282. DOI:10.1002/qj.2037

Chan, K. T. F., and J. C. L. Chan, 2016: Sensitivity of the simulation of tropical cyclone size to microphysics schemes. *Adv. Atmos. Sci*., **33**(9), 1024-1035, doi: 10.007/200376-0165183-2.

Corderia, J. M., Ralph, F. M., Martin, A, Gaggini, N., Spackman, J. R., Neiman, P. J., Rutz, J. J., and Pierce, R: Forecasting atmospheric rivers during CalWater 2015. *Bull. Amer. Met. Soc.*, **98**, 449-459, DOI: 10.1175/BAMS-D-15-00245.1.

Dettinger, M. D., and D. Cayan, 2014: Drought and the California delta – A matter of extremes. *San Francisco Estuary Watershed Sci*., 12(2), 1-6. Available online at https://escholarship.org/uc/item/88f1j5ht.

Di Liberto, T. (30 January 2017) Soaking rains and massive snows pile up in California I January 2017. Retrieved from https://www.climate.gov/news-features/event tracker/soaking-rains-and-massive-snows-pile-california-january-2017.

Dirren S., M. Didone, H. C. Davies, 2003: Diagnosis of 'forecast-analysis' differences of a weather prediction system. *Geophys Res. Lett.*, **30**, 2060-2063, DOI:10.1029/2003GL017986.

Dudhia, J, 2017: Overview of WRF physics [PowerPoint slides]. Retrieved from http://www2.mmm.ucar.edu/wrf/users/tutorial/201707/physics.pdf

Gram, C. M., and Archambault, H. M., 2016: The key role of diabatic outflow in amplifying the midlatitude flow: A representative case study of weather systems surrounding western north pacific extratropical transition. *Mon. Wea. Rev.*, **144**, 3847-3869, DOI: 10.1175/MWR-D-15-0419-1.

Gray, S. L., C. M. Dunning, J. Methven, G. Masato, and J. M. Chagnon, 2014: Systematic model forecast error in Rossby wave structure. *Geophys. Res. Lett.*, 41, 2979–2987, doi:10.1002/2014GL059282.

Grell, G. A. and S. R. Freitas, 2014: A scale and aerosol aware stochastic convective parameterization for weather and air quality modeling. *Atmos. Chem. Phys.*, **14**, 5233-5250, doi:10.5194/acp-14-5233-2014.

Hong, S. -Y., J. Dudhia, and S.-H. Chen, 2004: A revised approach to ice microphysics processes for the bulk parameterization of clouds and precipitation. *Mon. Wea. Rev.*, **132**, 103-120, doi: 10.1175/1520-0493(2004)132<0103:ARATIM>2.0CO;2.

--------, and Y. Noh, and J. Dudhia, 2006: A new vertical diffusion package with an explicit treatment of entrainment processes. *Mon. Wea. Rev.*, **134,** 2318–2341.

Janjic, Z. I., 1994: The step-mountain eta coordinate model: further developments of the convection, viscous sublayer and turbulence closure schemes, *Mon. Wea. Rev.*, **122**, 927–945.

Joos H., H. Wernli, 2012. Influence of microphysical processes on the potential vorticity development in a warm conveyor belt: a case-study with the limited-area model COSMO. *Q. J. R. Meteorol. Soc.,* **138**, 407–418. DOI:10.1002/qj.934

--------, R. M. Forbes, 2016: Impact of different IFS microphysics on a warm conveyor belt and the downstream flow evolution. *Q. J. R. Meteorol. Soc.*, **142**, 2727-2739, DOI:10.1002/qj/2863.

Kain, J. S., 2004: The Kain-Fritsch convective parameterization: An update. *J. Appl. Meteor.*, **43**, 170-181.

Kalnay, E., et al., 1996: The NCEP/NCAR 40-year reanalysis project. *Bull. Amer. Meteor. Soc.*, **77**, 437-471.

Kessler, E., 1995: On the continuity and distribution of water substance in atmospheric circulations. *Atmospheric Research*, **38**, 109-145, doi:10.1016/01698095(94)00090-Z.

Knippertz, P. and J. E. Martin, 2007: A Pacific moisture conveyor belt and its relationship to a significant precipitation event in the semiarid southwestern United States. *Wea. And Forec.*, **22**, 125-144, DOI: 10.1175/WAF963.1.

Madonna, E., H. Wernli, H. Joos, and O. Maritus, 2013: Warm conveyor belts in the ERA-Interim dataset (1979-2010). Part I: Climatology and potential vorticity evolution. *J. Climate.*, **27**, 3-26.

---------, E., S. Limbach, C. Aebi, H. Joos, H. Wernli, and O. Martius, 2014: On the co-occurrence of warm conveyor belt outflows and PV streamers. *J. Atmos. Sci.*, **71**, 3668-3673.

Martinez-Alvarado, O., E. Madonna, S. L. Gray and H. Joos, 2015: A route to systematic error in forecasts of Rossby waves. *Q. J. R. Meteorol. Soc.,* **142**, 196-210. DOI:10.1002/qj.2645.

Martius, O., E. Zenklusen, C. Schwierz, and H. C. Davies, 2006: Episodes of Alpine heavy precipitation with an overlying elongated stratospheric intrusion: A climatology. *Int. J. Climatol.*, **26**, 1149-1164.

--------, C. Schwierz and H. C. Davies, 2007: Breaking waves at the tropopause in the wintertime Northern Hemisphere: Climatological analyses of the orientation and the theoretical LC1/2 classification. *J. Atmos. Sci.*, **64**, 2576-2592. DOI: 10.1175/JAS3977.1

--------, C. Schwierz, and H. C. Davies., 2008: Far-upstream precursors of heavy precipitation events on the Alpine south-side. *Q. J. R. Meteorol. Soc.*, **134**: 417–428

Martin, J. E., Vavrus, S. J., F. Wang, and J. A. Francis, 2016: Sinuosity as a measure of middle tropospheric waviness. Unpublished manuscript. Available at http://marrella.aos.wisc.edu/.

Massacand, A. C., H. Wernli, and H. C. Davies, 1998: Heavy precipitation on the Alpine southside: An upper-level precursor. *Geophs. Res. Lett.*, **25**, 1435-1438.

---------, H. Wernli, and H. C. Davies, 2001: Influence of upstream diabatic heating upon an Alpine event of heavy precipitation. *Mon. Wea. Rev.*, **129**, 2822-2828.

Nieto, R., L. Gimeno, L. De La Torre, P. Ribera, D. Gallego, R. García-Herrera, J. Agustín García, M. Ruñez, A., Redaño, J. Lorente, 2005: Climatological features of cutoff low systems in the Northern Hemisphere. *J. Climate*, **18**, 3085-3103.

Leopold, L. B., M. G. Wolman, and J. Miller, 1964: *Fluvial process in geomorphology*. W. H. Freeman & Co., San Francisco, 522 p.

Pan, H. L., and W. S. Wu., 1995: Implementing a mass flux convective parameterization package for the NMC medium range forecast model. *NMC office note*, **409.40**, 20-233.

Pfahl, S., Schwierz, C., Croci-Maspoli, M., Grams, C. M., and Wernli, H, 2015: Importance of latent heat release in ascending air streams for atmospheric blocking. *Nature Geosci*., **8**, 610-615, DOI: 10.1038/NEGO2487

Pleim, J. E., 2007: A combined local and non-local closure model for the atmospheric boundary layer. Part 1: Model description and testing, *J. Appl. Meteor. and Clim*., **46**, 1383–1395.

Ralph, F. M., Kawzenuk, B., Hecht, C., and Kalansky, J. (2017, April 6). How many atmospheric rivers have hit the U.S. west coast during the remarkably wet water year 2017? Retrieved from http://cw3e.ucsd.edu/.

Rodwell, M. J., Magnusson, L., Bauer, P., Betchtold, P., Bonavita, M., Cardinali, C., Diamantakis, M., Earnshaw, P., Garcia-Mendez, A., Isaksen, L., Kallen, E., Kloche, D., Lopez, P., McNally, T., Perrson, A., Prates, F., and Wedi, N., 2013: Characteristics of occasional poor medium-range weather forecasts for Europe. *Bull. Amer. Soc.*, **94**, 393-1405.

Rogers, E., T. Black, B. Ferrier. Y. Lin, D. Parrish and G. DiMego, 2001: Changes to the NCEP Meso Eta Analysis and Forecast System: Increase in resolution, new cloud microphysics, modified precipitation assimilation, modified 3DVAR analysis. Available online at http://www.nws.noaa.gov/om/tpb/447body.htm.

Röthlisberger, M., Pfahl, S., and Martius, O., (2016): Regional-scale jet waviness modulates the occurrence of midlatitude weather extremes. *Geo. Phys. Res. Lett*., **43**(20), 989-997.

Skamarock, W. C., J. B. Klemp, J. Dudhia, D. O. Gill, D. M. Barker, M. G. Duda, X. Huang, W. Want, J. G. Powers, 2008: A Description of the Advanced Research WRF Version 3. *NCAR Technical Note*.

Stoelinga, M. T., 1995: A potential vorticity-based study of the role of diabatic heating and friction in a numerically simulated baroclinic cyclone. *Mon. Wea. Rev.*, **124**, 849-874.

Thorncroft, C. D., B. J. Hoskins, and M. E. McIntyre, 1993: Two paradigms of baroclinic-wave life-cycle behaviour. *Q. J. R. Meteorol. Soc*, **119**, 15-55.

Weather Research and Forecasting Model, 2018. Retrieved from https://www.mmm.ucar.edu/weather-research-and-forecasting-model